

**Shelf flows forced by deep-ocean anticyclonic eddies at the shelfbreak**

Deepak A. Cherian<sup>\*†</sup>

*Woods Hole Oceanographic Institution, Woods Hole, Massachusetts, USA*

K. H. Brink

<sup>5</sup> \*Current affiliation: College of Earth, Ocean and Atmospheric Sciences, Oregon State University,  
<sup>6</sup> Corvallis, Oregon, USA.

<sup>7</sup> <sup>†</sup>Corresponding author address: Deepak A. Cherian, 104 CEOAS Admin Building, Oregon State  
<sup>8</sup> University, Corvallis, OR 97333.

<sup>9</sup> E-mail: dcherian@coas.oregonstate.edu

## ABSTRACT

10 Isolated monopolar eddies in the ocean tend to move westward. Those shed  
11 by western boundary currents may then interact with the continental margin.  
12 This simple picture is complicated by the presence of other flow features, but  
13 satellite observations show that many western boundary continental shelves  
14 experience cross-shelfbreak exchange flows forced by mesoscale eddies trans-  
15 lating near the shelfbreak.  
16 Here we extend our previous study of eddy interaction with a flat shelf to that  
17 with a sloping shelf. Using a set of primitive-equation numerical simulations,  
18 we address the vertical structure of the onshore and offshore flows forced by  
19 the eddy, the origin of the exported shelf-water and the extent to which eddy  
20 water can penetrate on to the shelf. The simulations reveal an asymmetry in  
21 the vertical structure of cross-shelfbreak flows: the offshore flow is generally  
22 barotropic whereas the onshore flow is always baroclinic. The exported shelf  
23 water is sourced from downstream of the eddy in the coastal-trapped wave di-  
24 rection and is supplied by a barotropic along-shore jet. This “supply jet” has a  
25 Rhines-like cross-shore length scale proportional to (eddy-velocity-scale/shelf-  
26 topographic-beta)<sup>1/2</sup> measured from the shelfbreak. The eddy can force eddy  
27 water on to the shelf a distance of one internal Rossby deformation radius,  
28 defined using shelf properties, from the shelfbreak.  
29 We rationalize these horizontal and vertical scales, connect them to existing  
30 observations and extend our previous parameterization of eddy-forced offshore  
31 shelf-water flux to account for non-zero shelf slopes.

<sup>32</sup> **1. Introduction**

<sup>33</sup> Deep-water mesoscale anticyclonic eddies interact with continental shelf-slope topography in many  
<sup>34</sup> parts of the world: for example, the Mid-Atlantic Bight off the northeastern United States (Joyce  
<sup>35</sup> et al. 1992), the Gulf of Alaska (Okkonen et al. 2003), the east Australian shelf (Tranter et al. 1986)  
<sup>36</sup> and others. At the shelfbreak, these eddies export shelf water offshore (e.g., Figure 1 and Joyce et al.  
<sup>37</sup> 1992) while also transporting eddy and slope waters on to the shelf (e.g., Lee and Brink 2010; Zhang  
<sup>38</sup> and Gawarkiewicz 2015). Eddy-forced fluxes are one of many time-dependent mechanisms that  
<sup>39</sup> could accomplish the shelf-water export and deep-water import required to satisfy volume, heat and  
<sup>40</sup> salt budgets for the Mid-Atlantic Bight (Brink 1998; Lentz 2010). The relative importance of such  
<sup>41</sup> eddy-forced fluxes in satisfying these shelf budgets is still unconstrained (Cherian and Brink 2016).  
<sup>42</sup> In addition, there are biological implications to the export of shelf water — increased warm-core  
<sup>43</sup> ring activity at the Mid-Atlantic Bight shelfbreak has been linked to decreased recruitment for some  
<sup>44</sup> fish species (Myers and Drinkwater 1989).

<sup>45</sup> Beyond fluxes, eddy-interactions can substantially change water-mass and flow properties on the  
<sup>46</sup> outer shelf, at least temporarily. For example, Zhang and Gawarkiewicz (2015) studied satellite  
<sup>47</sup> and *in situ* observations of what they termed “Pinocchio’s Nose Intrusion”: an along-shelf gravity  
<sup>48</sup> current carrying warm salty Gulf Stream water downstream in the coastal-trapped wave sense  
<sup>49</sup> along the Mid-Atlantic Bight shelfbreak. Such a feature was previously noted in the numerical  
<sup>50</sup> experiments of Shi and Nof (1993) and Oey and Zhang (2004); and observed by Lee and Brink  
<sup>51</sup> (2010). The “intrusion” was forced by a Gulf Stream warm-core ring interacting with the shelf-slope  
<sup>52</sup> topography and was confined to a small region near the shelfbreak. The ring advected onshore a  
<sup>53</sup> density front usually present at this shelfbreak — generally termed a “shelfbreak front” (Linder and

<sup>54</sup> Gawarkiewicz 1998). In one dramatic example, Cenedese et al. (2013) observed a warm-core ring  
<sup>55</sup> forcing the reversal of the baroclinic jet that balances this shelfbreak density front. Such dramatic  
<sup>56</sup> changes need not always occur. Depending on their trajectory, the influence of warm-core rings can  
<sup>57</sup> be solely limited to the upper slope (Ramp et al. 1983; Beardsley et al. 1985).

<sup>58</sup> In this manuscript, we examine the flow field on a sloping shelf forced by a translating deep-water  
<sup>59</sup> mesoscale anticyclonic eddy present at the shelfbreak. As in the flat shelf study of Cherian and  
<sup>60</sup> Brink (2016), we use a series of idealized primitive equation numerical simulations in which an  
<sup>61</sup> anticyclonic eddy initialized in deep water moves toward and interacts with shelf-slope topography  
<sup>62</sup> to the south. There we studied the fate of shelf water parcels once they leave the shelf, and presented  
<sup>63</sup> a recipe for estimating the magnitude of the cross-shelfbreak transport. We expect the background  
<sup>64</sup> potential vorticity gradient associated with the bottom slope to substantially influence the structure  
<sup>65</sup> of the shelf's response to eddy forcing at the shelfbreak. Accordingly, our focus here is the flow  
<sup>66</sup> field on a *sloping* shelf. We tackle the following questions: (1) where in the along- and cross-isobath  
<sup>67</sup> directions does the exported shelf water originate, (2) to what extent can eddy water penetrate on to  
<sup>68</sup> the shelf, (3) are the cross-shelfbreak flows vertically uniform or vertically sheared, i.e. is shelf  
<sup>69</sup> water exported primarily from near the surface or from the bottom, and (4) does the magnitude of  
<sup>70</sup> offshore transport of shelf water depend on the shelf slope? We begin by describing the model.

## <sup>71</sup> 2. Experiment design

<sup>72</sup> The experiments are near-identical to those in Cherian and Brink (2016), so nearly all the material  
<sup>73</sup> below is repeated with minor modifications so that this manuscript is self-contained. The only  
<sup>74</sup> difference here is that the shelf is now sloping. We use an idealized configuration of the hydrostatic,

- 75 primitive equation Regional Ocean Modeling System (ROMS, Shchepetkin and McWilliams 2005).  
 76 It solves the equations (subscripts represent differentiation,  $\rho \equiv \rho_0 + \rho(x, y, z, t)$ , and  $\nabla = \partial_x \hat{i} + \partial_y \hat{j}$ ):

$$u_t + uu_x + vu_y + wu_z - fv = -\frac{1}{\rho_0} p_x + (A_v u_z)_z + \nabla \cdot (A_H \nabla u) + \underbrace{\nabla \cdot \sqrt{A_B} \nabla \left( \nabla \cdot \sqrt{A_B} \nabla u \right)}_{\text{biharmonic viscosity}} \quad (1)$$

$$v_t + uv_x + vv_y + wv_z + fu = -\frac{1}{\rho_0} p_y + (A_v v_z)_z + \nabla \cdot (A_H \nabla v) + \nabla \cdot \sqrt{A_B} \nabla \left( \nabla \cdot \sqrt{A_B} \nabla v \right) \quad (2)$$

$$0 = -p_z - \rho g \quad (3)$$

$$u_x + v_y + w_z = 0 \quad (4)$$

$$\rho_t + u\rho_x + v\rho_y + w\rho_z = (\kappa_v \rho_z)_z + \nabla \cdot (\kappa_H \nabla \rho) + \underbrace{\nabla \cdot \sqrt{\kappa_B} \nabla \left( \nabla \cdot \sqrt{\kappa_B} \nabla \rho \right)}_{\text{biharmonic diffusivity}} \quad (5)$$

- 77  $(x, y, z)$  define a right handed Cartesian coordinate system with  $x$  being along-isobath;  $y$ , cross-  
 78 isobath and  $z$ , depth. The model domain is a  $\beta$ -plane with  $f = f_0 + \beta y$ . The main elements of the  
 79 problem viz., shelf-slope topography, anticyclonic eddy, and ambient stratification, are all reduced  
 80 to the simplest possible form.

- 81 The topography is constructed using three straight lines to bound the shelf, the continental slope  
 82 and the deep ocean respectively. The deep ocean bottom is always flat. A four-point running  
 83 mean is applied six times to smooth the topography at the shelfbreak and slopebreak. The term  
 84 “shelfbreak” refers to the intersection of the shelf and continental slope; while “slopebreak” refers  
 85 to the intersection of the continental slope and the flat bottomed deep ocean.

- 86 Salinity is always a constant, and the linear equation of state involves potential temperature only.  
 87 The eddy is a radially symmetric, surface intensified, Gaussian temperature anomaly superimposed

<sub>88</sub> on background stratification ( $\bar{\rho}$ ), as

$$T_{\text{edd}} = T_{\text{amp}} \exp [-(r/L_0)^2 - (z/L^z)^2]. \quad (6)$$

<sub>89</sub>  $r$  is the radial distance from the eddy's center. The initial horizontal length scale,  $L_0$ , is specified  
<sub>90</sub> and the vertical scale is  $L^z = (f_0 L_0)/(N\sqrt{2})$ , where  $L_0/\sqrt{2}$  is the radius to maximum velocity. The  
<sub>91</sub> density anomaly is balanced by a cyclo-geostrophic velocity field determined after prescribing zero  
<sub>92</sub> velocity at the bottom. The ambient buoyancy frequency ( $N$ ) is always constant. The eddy always  
<sub>93</sub> starts in deep water far from the topography, approximately one deformation radius away from the  
<sub>94</sub> slopebreak (Figure 2), so that its initial evolution is as over a flat bottomed ocean (verified using a  
<sub>95</sub> flat bottom simulation). We let the eddy adjust to the  $\beta$ -plane in deep water before it impacts the  
<sub>96</sub> slope, unlike previous studies where the eddy is initialized over the slope (e.g., Oey and Zhang  
<sub>97</sub> 2004; Zhang and Gawarkiewicz 2015).

<sub>98</sub> Isolated anticyclonic eddies move southwestward on a  $\beta$ -plane (McWilliams and Flierl 1979; Mied  
<sub>99</sub> and Lindemann 1979; Nof 1983; Early et al. 2011); making the eddy translate across isobaths  
<sub>100</sub> without a cross-isobath background flow. The southwestward motion renders two coastal locations  
<sub>101</sub> moot: for a coast at the north or east, the eddy will move away from the shelfbreak. So, the  
<sub>102</sub> topography must be placed at either the western or southern boundary of the domain for the eddy  
<sub>103</sub> to encounter it. *All experiments described here use topography with a southern coast.* With open  
<sub>104</sub> eastern and western boundaries, this configuration allows westward-propagating Rossby waves  
<sub>105</sub> radiated by the eddy (Flierl et al. 1983) to exit the domain; allowing the eddy to interact with  
<sub>106</sub> *undisturbed* shelf-slope waters. A western coast configuration traps Rossby wave momentum that  
<sub>107</sub> results in large flow features spinning up over the slope prior to the eddy's arrival (their Section  
<sub>108</sub> 9a Cherian and Brink 2016). Upon impact, the eddy then translates northward toward these flow

109 features. Our goal here is to study the shelf-edge flows that results from the interaction of an  
110 isolated eddy with undisturbed shelf-slope waters and such northward translation is not desirable.  
111 Qualitatively, our results hold for both orientations because the shelf-edge flows of interest have  
112 horizontal length scales too small to be influenced by the planetary  $\beta$ -plane. Quantitatively, the  
113 diagnosed length scales of shelf flows only differ by 2-3 grid points when comparing a simulation  
114 with a southern coast to that with a western coast (all other aspects being identical). In addition, the  
115 background topographic vorticity gradient on the shelf is usually a factor of 10-1000 larger than  
116 planetary  $\beta$  (compare  $\beta_{sh}$  and  $\beta$  in Table 2;  $\beta_{sh}/\beta \sim 100$  for the Middle-Atlantic Bight). Thus in  
117 realistic contexts the shelf's topographic  $\beta$ -plane is the primary background PV gradient. Coastal  
118 orientation then ceases to matter and the primary effect of the planetary  $\beta$ -plane is to make the eddy  
119 self-advect itself toward the topography.

120 The coastal boundary is a free-slip wall. The other three boundaries are open. Boundary conditions  
121 used at these open boundaries are an explicit Chapman condition for the free-surface (Gravity Wave  
122 Radiation: Explicit in Chapman 1985), a modified Flather condition for 2D momentum (Mason et al.  
123 2010) and a combined radiation-nudging condition for tracers and 3D momentum (Marchesiello  
124 et al. 2001). We use sponge layers to prevent noise at the open boundary from contaminating the  
125 solution. These are 50 km (40 points) wide regions with lateral Laplacian viscosity ( $A_H$ ) linearly  
126 increasing from 0 to  $50 \text{ m}^2 \text{ s}^{-1}$  and lateral Laplacian diffusivity  $\kappa_H = 0\text{--}5 \text{ m}^2 \text{ s}^{-1}$ .

127 For computational efficiency, a hyperbolic tangent function is used to stretch the horizontal grid  
128 spacing near the sponge layers at the open boundaries. Horizontal spacing is always at least 1 km  
129 and less than 2.5 km. Our diagnostics are not very sensitive to changes in grid spacing. In the  
130 vertical, we distribute 72 grid points such that vertical grid spacing is smallest near the surface  
131 and largest near the bottom (0.6–25 m). A density Jacobian based algorithm (Shchepetkin and

132 McWilliams 2003) reduces pressure gradient error<sup>1</sup>. We use biharmonic lateral viscosity ( $A_B =$   
 133  $4.4 \times 10^6$ – $3 \times 10^8 \text{ m}^4 \text{ s}^{-1}$ ) and diffusivity ( $\kappa_B = 1.2 \times 10^3$ – $8 \times 10^4 \text{ m}^4 \text{ s}^{-1}$ ) along sloping vertical  
 134 co-ordinate surfaces<sup>2</sup> to control noise outside the sponge layers. The values scale with grid cell  
 135 size. The Laplacian coefficients  $A_H, \kappa_H$  are 0 outside the sponge layers. When used, the bottom  
 136 friction term is linear,

$$\boldsymbol{\tau}^{\text{bot}} = \rho_0 r_f(u, v). \quad (7)$$

### 137 3. Diagnostics

#### 138 a. Topography

139 The topography is characterized by the following parameters.  $\lambda = H_{\text{sb}}/L^z$  is a non-dimensional  
 140 measure of the shelfbreak depth  $H_{\text{sb}}$  relative to the eddy's vertical scale  $L^z$ . A slope Burger number  
 141 is defined as  $S = \alpha N/f_0$  with  $\alpha = dH/dy$  and subscripts ‘sh’, ‘sl’ referring to the continental  
 142 shelf and continental slope respectively. Topographic  $\beta$  for the shelf is defined as  $\beta_{\text{sh}} = \alpha_{\text{sh}} f_0 / H_{\text{sb}}$ .  
 143 Finally,  $Y_{\text{sb}}$  will refer to the y-location of the shelfbreak.

#### 144 b. Eddy diagnostics

145 The eddy is tracked using the method described in Chelton et al. (2011) with slight modifications.  
 146 The method detects a largest possible simply connected region within a closed SSH contour  
 147 containing a SSH maximum (or minimum for a cyclone). The eddy's center  $(x_{\text{cen}}(t), y_{\text{cen}}(t))$  is  
 148 defined as the location of the SSH maximum within the detected region. The core of the eddy is

<sup>1</sup>ROMS option DJ\_GRADPS

<sup>2</sup>s-surfaces in ROMS terminology

149 defined as the zero relative vorticity contour within the detected SSH boundary. Despite concerns  
150 raised by Beron-Vera et al. (2013) and others, the detected eddy boundary does enclose material  
151 that is trapped over large space and time scales and is deemed to be a useful diagnostic (e.g. Figure  
152 2 and Early et al. 2011).

153 Time series of the eddy's velocity and length scales are obtained by assuming that the eddy's  
154 density anomaly remains a Gaussian in all dimensions throughout the simulation. At the surface,  
155 the density field is  $(\rho_e \exp[-(r/L_0(t))^2])$ . The corresponding balanced geostrophic velocity field,  
156 with maximum velocity  $V_0$ , is described by

$$V = (\sqrt{2e}) V_0 \left( \frac{r}{L_0} \right) e^{-(r/L_0)^2}. \quad (8)$$

157 Equation (8) is fit to the eddy's surface velocity along a horizontal line in the along-isobath direction.  
158 The fit determines the eddy's maximum azimuthal velocity  $V_0$  and its Gaussian length scale  $L_0$   
159 at the latitude of the eddy's center. These metrics, though based on approximations about eddy  
160 shape, are much less sensitive than estimating average velocities along an identified contour or the  
161 contour's equivalent radius. A Gaussian fit,  $\exp[-(z/L^z)^2]$ , to the vertical profile of the temperature  
162 anomaly at the eddy's center diagnoses its vertical scale  $L^z$ . The eddy's Rossby number is defined  
163 as  $\text{Ro}(t) = V_0(t)/[f_0 L_0(t)]$ . The eddy's eastern and western edges are defined as  $x_{\text{cen}}(t) \pm L_0(t)$   
164 respectively.

165 *c. Time interval for averaging*

166 We will examine flow fields and scales averaged over a time interval when the eddy is interacting  
167 with the shelf and slope. As in Cherian and Brink (2016), we define that time interval using the

<sub>168</sub> cumulative integral of the cross-shelfbreak flux of shelf water. We will use the notation  $[t_{\text{start}}, t_{\text{stop}}]$ ,  
<sub>169</sub> where  $t_{\text{start}}$  ( $t_{\text{stop}}$ ) are the times at which the accumulated shelf-water volume transported across the  
<sub>170</sub> shelfbreak is 5% (95%) of its value at the end of the simulation.

<sub>171</sub> *d. Vertical structure of flows*

<sub>172</sub> The non-dimensional parameter

$$BC = \text{median} \left\{ \frac{|U_s - U_b|}{|U_s|} \right\} \quad (9)$$

<sub>173</sub> quantifies the extent to which a velocity field is vertically sheared i.e., baroclinic.  $U_s$  and  $U_b$  are  
<sub>174</sub> velocities at the surface and 10 points off the bottom respectively. The definition prevents BC from  
<sub>175</sub> being substantially influenced by the bottom boundary layer in simulations with bottom friction.  
<sub>176</sub> For barotropic flows,  $U_s = U_b$  and  $BC = 0$ ; whereas for more baroclinic flows,  $U_s U_b < 0$  or  $U_b = 0$   
<sub>177</sub> and  $BC \geq 1$ . We restrict the calculation to only include cells with  $|U_s| \geq 0.2 \max \{|U_s|\}$ , the spatial  
<sub>178</sub> maximum being calculated at each time instant. We will use this metric separately with along- and  
<sub>179</sub> cross-shelf velocities over the shelf, i.e. with  $U \equiv u$  and  $U \equiv v$  respectively. When a time series of  
<sub>180</sub> BC is required (i.e. in Section 7), the median will only be applied in  $(x, y)$ .

<sub>181</sub> *e. Water masses*

<sub>182</sub> There is *no* shelfbreak front, so shelf and slope waters are indistinguishable in density. Instead,  
<sub>183</sub> each water parcel is tagged with its initial latitude using a passive tracer termed the “cross-shelf  
<sub>184</sub> dye”  $C(x, y, z, t)$ ;  $C(x, y, z, t = 0) = y$ . This dye traces “shelf water”: water parcels that initially start  
<sub>185</sub> south of the shelfbreak  $C(x, y, z, t) < Y_{\text{sb}}$ , the latitude of the shelfbreak; and “slope water”: parcels  
<sub>186</sub> that are initially between the shelf- and slope-break.

187 We use a second passive tracer  $E(x, y, z, t)$  to track water parcels in the eddy. This passive tracer is  
188 initialized with value 1 where the temperature anomaly (6) is greater than some small value; and 0  
189 elsewhere. In practice, not all of the dye with value 1 is carried with the eddy, but this conservative  
190 initial distribution lets us identify an eddy core that transports mass over long spatial and time  
191 scales. In addition, the eddy also homogenizes the cross-shelf dye within it, letting us distinguish it  
192 from the surrounding water. We will define water parcels with  $E > 0.7$  to be “eddy water”. Thus  
193 the shelf-water and eddy-water boundaries are defined as  $C(x, y, z, t) = Y_{\text{sb}}$  and  $E(x, y, z, t) = 0.7$ .

## 194 4. Qualitative aspects

### 195 a. A typical simulation

196 The evolution of an anticyclone of radius 25 km, vertical scale 400 m and Rossby number 0.1 is  
197 visualized using the cross-shelf dye field in Figure 2. The slope Burger number for the continental  
198 slope is 1 and that of the shelf is 0.05. The shelfbreak depth is 50 m and there is no bottom friction.

199 The eddy evolves as described in Cherian and Brink (2016) for simulations with a flat shelf. It  
200 moves southwestward while radiating Rossby waves, evidenced by the westward spreading of SSH  
201 contours in Figure 2b. When its edge reaches the shelfbreak, the eddy translates westward along an  
202 isobath, continuously leaking mass in an along-shelfbreak jet (Figure 2c-f), termed the “leakage”  
203 by Shi and Nof (1993) and “Pinocchio’s Nose Intrusion” by Zhang and Gawarkiewicz (2015). The  
204 along-isobath scale of both off- and on-shore flow at the shelfbreak is an eddy radius; apparent in  
205 Figure 3: the  $x$ - $t$  Hovmöller diagram of depth-averaged cross-isobath flow at the shelfbreak. Figure

<sup>206</sup> 3 does not distinguish between eddy and shelf waters. The solid black line is the eddy center and  
<sup>207</sup> the dashed lines are the eddy's western and eastern edges.

<sup>208</sup> The eddy exports shelf water across the shelfbreak while advecting slope and eddy waters on to the  
<sup>209</sup> shelf. Initially, the shelf water is exported as a filament, termed a "streamer" in the literature (Figure  
<sup>210</sup> 2d). Later, the exported shelf water forms cyclones that then combine with eddy water in the leakage  
<sup>211</sup> to form dipoles (Figure 2e,f). These cyclones are "stacked" — they contain shelf water stacked over  
<sup>212</sup> eddy water with cyclonic vorticity throughout. Cherian and Brink (2016) described their formation  
<sup>213</sup> as a consequence of instability waves excited on the eddy's potential vorticity gradient when it  
<sup>214</sup> impacts the continental slope. These consist of a growing cyclonic anomaly propagating on the  
<sup>215</sup> eddy's edge and a growing anticyclonic anomaly propagating in the eddy's core. The cyclonic  
<sup>216</sup> anomaly traps shelf water advected over it as it grows to finite amplitude and ultimately forms a  
<sup>217</sup> "stacked cyclone". Cherian and Brink (2016) explain this process in more detail. Here we study the  
<sup>218</sup> shelf flow field forced by the eddy. A shelf volume budget and the schematized flow field in Figure  
<sup>219</sup> 4 will provide useful context for the rest of our investigation.

<sup>220</sup> b. *Volume budget for the shelf*

<sup>221</sup> A volume budget for "shelf water" may be constructed in two ways. First, consider shelf-water as  
<sup>222</sup> water parcels in a fixed geographic volume bounded by the shelfbreak and the coast to the south. As  
<sup>223</sup> expected from the linear physics described in Chapman and Brink (1987), the eddy's influence on  
<sup>224</sup> the shelf is largely to the east (i.e. downstream of the eddy in the coastal-trapped wave sense; Figure  
<sup>225</sup> 4). The *net* offshore volume flux across the shelfbreak is compensated by an along-shelf input to  
<sup>226</sup> the shelf at the open eastern boundary — solid and dashed black lines nearly balance in the shelf

volume budget (Figure 5). This approximate balance holds regardless of shelf slope magnitude and orientation (southern or western coast<sup>3</sup>). The eastern boundary is special in this configuration because it is the “downstream” boundary, relative to the propagation direction of coastal-trapped, or Kelvin, waves. The volume of water on the shelf, again defined geographically, does not change appreciably throughout the simulation.

Second, consider shelf water to be water parcels defined using a water property such as salinity. The simulations here lack salinity; so shelf water is defined as parcels with initial cross-shelf dye value  $< Y_{sb}$  i.e. these are water parcels that started on the shelf at  $t = 0$ . This definition of shelf water is used for the rest of the paper. The eddy exports shelf water, so defined, across the shelfbreak. To compensate, an along-shelf “supply jet” directed westward (upstream) toward the eddy supplies shelf water from the open eastern (downstream) boundary (Figure 4). Again up- and down-stream are directions relative to the coastal-trapped- or Kelvin-wave propagation direction. The compensation is always incomplete: the cross-shelf export of shelf water is larger than the along-shelf import of shelf water by about 30% in Figure 5 (compare solid and dashed blue lines). The rest is compensated by the onshore transport of eddy- and slope-waters. There is thus permanent export of shelf water. Shelf water parcels that cross the shelfbreak never return to the shelf; they are trapped in the “stacked cyclones” described in Cherian and Brink (2016). Further, the along-shelfbreak eddy-water leakage (or intrusion) also prevents exported shelf water parcels returning to the shelf (Figure 2d–f). Simulations with a western coast exhibit analogous behaviour: a northward along-shelf jet supplies shelf water from downstream (now south) of the eddy (Cherian and Brink 2016). Such behaviour agrees with the linear simulations of Chapman and Brink (1987).

---

<sup>3</sup>We rely on western coast simulations from Cherian and Brink (2016)

248 c. Instantaneous flow field

249 The instantaneous flow fields over the shelf exhibit significant complexity: see snapshots at  
250  $t = 300$  days in Figure 6). Figure 6b is a snapshot of the cross-shelfbreak flow with density contours  
251 overlaid in black. The blue contours bound water parcels that started inshore of the shelfbreak. The  
252 offshore flow of shelf water is concentrated near the eddy ( $x \approx 150$  km). There is a strong density  
253 front between eddy and shelf waters, and associated vertical shear. This shear largely affects eddy  
254 water parcels and the offshore flow of shelf water is largely barotropic ( $BC \sim 0.1$ ). In contrast, the  
255 onshore flux of eddy water is accomplished by a vertically-sheared cross-shelf flow near the eddy  
256 ( $BC \sim 0.9$ ;  $x \approx 180$  km in Figure 6b).

257 Figure 6c,d are both cross-shelf sections of the along-shelf velocity at  $x = 350$  km; the only  
258 difference being that Figure 6c focuses on the shelf while Figure 6d focuses on the outer slope.  
259 The along shelf supply jet is evident at  $y \approx 30$  km. Again the blue (red) contours indicate the  
260 shelf-water (eddy-water) boundary. Here too is a density front with the associated vertical shear  
261 largely experienced by eddy-water parcels. The along-shelf flow of shelf-water toward the eddy  
262 is largely barotropic and confined to a narrow region near the shelfbreak (in to the plane, *inshore*  
263 of the blue contour,  $y \approx 30$  km in Figure 6c,d). This “supply jet” supplies the shelf water that is  
264 exported across the shelfbreak from the eastern boundary of the shelf. The eddy-water leakage is  
265 surface intensified (*offshore* of the blue contour,  $y \approx 40$  km in Figure 6c,d). A near-bottom velocity  
266 maximum is evident over the upper slope (Figure 6d). This “slope jet” transports eddy waters  
267 downstream in the coastal-trapped wave direction and has been studied in detail by Oey and Zhang  
268 (2004).

269 *d. Comparison with flat shelf simulations*

270 When qualitatively compared to a flat shelf, a sloping shelf reduces both

271 1. the cross-isobath extent of the supply jet, and

272 2. the magnitude of offshore shelf-water transport.

273 Both effects are evident when comparing an instantaneous snapshot of the surface dye field and

274 surface velocity vectors to an analogous snapshot from a simulation with a flat shelf (Figure 7).

275 Over a flat shelf, the supply jet exists across the whole shelf (Figure 7a) while the sloping shelf

276 reduces the supply jet's cross-isobath length scale. This limited cross-isobath scale is an inertial

277 length scale:  $L_\beta = \sqrt{V_0/\beta_{\text{sh}}}$ ,  $V_0$  being an eddy velocity scale and  $\beta_{\text{sh}} = f_0/H_{\text{sb}} \alpha_{\text{sh}}$ , topographic

278 beta for the shelf (see Section 5b).

279 Time series of the cross-shelfbreak flux of shelf water are presented in Figure 8a. The flux is

280 calculated by integrating the cross-shelfbreak velocity field over shelf-water parcels identified

281 as such using the cross-shelf dye field ( $C(x, Y_{\text{sb}}, z, t) \leq Y_{\text{sb}}$ ). Relative to a flat shelf simulation, a

282 sloping shelf reduces both peak and average cross-shelfbreak flux magnitudes (compare dark red

283 and dark blue lines in Figure 8a). We will argue that the reduced offshore flux is a consequence of

284 the limited cross-shelf extent of the eddy's influence (Section 6). First we study the horizontal and

285 vertical scales of eddy-forced flows on the shelf.

286 **5. Flow on the shelf**

287 *a. Average cross-shelfbreak flows*

288 The eddy's effect on water properties and tracers over the outer shelf will depend on the vertical  
289 structure of cross-shelfbreak flows it forces. Accordingly, we now examine *average* vertical profiles  
290 of the offshore flow of shelf water and the onshore flow of eddy- and slope-waters at the shelfbreak.  
291 We construct these profiles using the instantaneous cross-shelf dye and cross-isobath velocity  
292 fields (for e.g. Figure 6b). The velocity field is integrated in the along-isobath direction  $x$  and  
293 over  $[t_{\text{start}}, t_{\text{stop}}]$  to obtain a vertical profile, after restricting the domain to comprise only shelf or  
294 non-shelf (eddy- and slope-water) water parcels.

295 First consider the onshore flow of eddy- and slope-waters. The instantaneous cross-shelfbreak  
296 velocity field for  $x \gtrsim 180\text{ km}$  contains many zero crossings (Figure 6b). A simple average will only  
297 reflect the degree to which the positive and negative velocities cancel out, obscuring our view of the  
298 flow's vertical structure. We construct a more useful average by imposing two restrictions:

299 1. We use only onshore velocities when integrating over eddy- and slope-water parcels. For  
300 consistency, we similarly restrict ourselves to only offshore velocities when integrating over  
301 shelf water parcels<sup>4</sup>.

302 2. We restrict our along-shelf integration to  $x_{\text{cen}} - 1.2L_0 \leq x \leq x_{\text{cen}} + 1.2L_0$ ,  $x_{\text{cen}}$  being the along-  
303 shelf location of the eddy's center and  $L_0$  being the eddy's initial radius. The decision follows  
304 from Figure 3 where substantial offshore and onshore flows largely occur within a radius of  
305 the eddy's center, when depth-averaged.

---

<sup>4</sup>Integrating over shelf parcels with both offshore and onshore velocities results in minor quantitative differences.

306 The averaged profiles calculated from a set of inviscid simulations are presented in Figure 9. The  
307 parameters varied include shelf slope, eddy velocity and length scales, and shelfbreak depth (Table  
308 2). The vertical variation in each profile reflects the vertical variation in both velocity and dye  
309 fields (Figure 6b). The *average* vertical structure of offshore “outflow” of shelf water and the  
310 onshore “inflow” of eddy- and slope-water across the shelfbreak differ for the same simulation. The  
311 eddy- and slope-water inflow is always vertically sheared or baroclinic (Figure 9b). In contrast, the  
312 export of shelf water is generally vertically uniform or barotropic with some exceptions (Figure 9a).  
313 Strikingly, differences in vertical structure of the shelf water outflow are seen even when the ratio  
314 of shelfbreak depth to eddy vertical scale  $\lambda = H_{\text{sb}}/L^z$ , i.e. shelf vertical scale to forcing vertical  
315 scale, is unchanged. The profiles highlighted in red in Figure 9a are from two simulations with  
316  $\lambda = 0.22^5$ . One is significantly more barotropic than the other. These structures and their variation  
317 will now be rationalized. We will address the flow of shelf water and non-shelf waters separately,  
318 beginning with the supply of shelf water parcels from the eastern boundary.

319 *b. The flow of shelf water*

320 1) THE ALONG-SHELF SUPPLY JET

321 In the following, we develop a scaling argument for the cross-shelf scale of the along-shelf supply  
322 jet. We will ignore the presence of eddy- and slope-water parcels on the shelf because these parcels  
323 occupy a minor portion of the shelf in Figure 6a,c.

324 The instantaneous snapshots make it clear that the along-shelf supply jet is dominantly barotropic  
325 or vertically uniform. (Figure 6d). So guided, we ignore the density field in developing a scaling

---

<sup>5</sup>ew-8381 and ew-8392 in Table 2

326 for the jet's width. The dynamics of the jet is then governed by the equation for vertical relative  
 327 vorticity,  $\zeta = v_x - u_y$  (Pedlosky 1987):

$$\frac{D}{Dt}(f + \zeta) = (f + \zeta) \frac{\partial w}{\partial z} + \frac{1}{\rho_0} \nabla \times \tau_z + \text{tilting terms.} \quad (10)$$

328 (10) can be integrated vertically between the surface and bottom to obtain (assuming steady flow,  
 329 ignoring tilting terms and using the bottom boundary condition,  $w = -\alpha_{sh}v^{bot}$ ):

$$\frac{1}{H} \int_{-H}^0 u \cdot \nabla(f + \zeta) dz = \beta_{sh} v^{bot} \left( 1 + \frac{\zeta}{f} \right) - \frac{r_f}{H} \zeta^{bot}. \quad (11)$$

330 For *inviscid* simulations, the scale of the jet is set by the balance between the first two terms. We  
 331 assume that both the depth-averaged along-shelf velocity and the bottom velocity  $v^{bot}$  are both  
 332 proportional to the eddy velocity scale  $V_0$ , i.e. the forcing scale, and that the  $(1 + \zeta/f)$  is  $O(1)$   
 333 for scaling purposes. Scaling both sides of the equation results in a horizontal length scale for the  
 334 supply jet,

$$L_\beta = O \left( \sqrt{\frac{V_0}{\beta_{sh}}} \right) \quad (12)$$

335 We are hypothesizing that the advection of relative vorticity balances the stretching caused by shelf  
 336 water parcels moving across isobaths as they cross the shelfbreak. This is a turning radius argument:  
 337 as the supply jet turns to cross the shelfbreak, its anticyclonic curvature balances the cyclonic  
 338 vorticity created by near-bottom stretching. We test the length scale in (12) using simulations where  
 339  $\lambda = H_{sb}/L^z < 0.35^6$  (Table 2). This is the relevant parameter range for Gulf Stream warm-core  
 340 rings at the Middle Atlantic Bight ( $\lambda \approx 0.1$ ).

341 To quantify the cross-shelf distance over which the eddy can extract shelf water, we record the  
 342 lowest value of cross-shelf dye crossing the shelfbreak,  $C_{min}(t) = \min_{x,z} C(x, Y_{sb}, z, t)$  (Figure 8b).

---

<sup>6</sup>When  $\lambda \geq 0.35$ , the shelfbreak is deep enough that a substantial portion of the eddy crosses on to the shelf. The eddy can then extract shelf water parcels from a distance larger than  $L_\beta$  from the shelfbreak (Cherian 2016, his Figure 6.10). Such simulations are not examined further.

343  $C_{\min}(t)$  identifies the origin of the most-onshore water parcel crossing the shelfbreak at a given  
 344 time instant. It is a measure of the cross-shelf extent of the eddy's influence. Over a flat bottom  
 345 (dark red), there is no dynamical limit and the value slowly increases with time until the flow  
 346 covers the entire shelf (shelf width is slightly smaller than eddy radius here). Over a sloping shelf,  
 347  $C_{\min}(t)$  asymptotes out, indicating a cross-shelf limit to the eddy's influence. We fit the function  
 348  $y_1 + y_0 \tanh[(t - t_0)/T]$  to  $C_{\min}(t)$ , with  $y_0, y_1, t_0, T$  being constants. The width of the supply jet is  
 349 estimated as  $|y_0 + y_1 - Y_{\text{sb}}|$ . This diagnosed width of the along-shelf supply jet varies linearly with  
 350 the length scale  $L_\beta = \sqrt{V_0/\beta_{\text{sh}}}$  (Figure 10a). On average, the eddy can extract a water parcel that  
 351 starts a distance of roughly  $1.22L_\beta$  away from the shelfbreak.

352 We emphasize that  $1.22L_\beta$  is, strictly speaking, a scale for the cross-shelf extent of the eddy's  
 353 influence measured from the shelfbreak (Figure 4). There are eddy- and slope-water parcels that  
 354 occupy a relatively minor portion of this zone of influence (Figure 6a,c). Section 5c1 will address  
 355 the width of the near-shelfbreak region occupied by the eddy- and slope-water parcels.

356 One can define a Burger number  $\varphi_o$  that compares the supply jet length scale  $L_\beta$  to the shelf  
 357 deformation radius (Burger 1958):

$$\varphi_o = \left( \frac{H_{\text{sb}}}{f_0 L_\beta / N} \right)^2 = \left( \frac{N H_{\text{sb}} / f_0}{L_\beta} \right)^2. \quad (13)$$

358  $\varphi_o$  indicates whether the baroclinic nature of a balanced along-isobath jet of width  $L_\beta$  is evident  
 359 over a shelf with depth  $O(H_{\text{sb}})$ . Over all simulations, the level of baroclinicity of the along-shelf  
 360 flow, BC defined in (9), varies approximately linearly with  $\varphi_o$  for  $\varphi_o \lesssim 0.35$  (Figure 9c). As  $\varphi_o$   
 361 increases, the shelf water supply jet appears increasingly sheared in the vertical because the shelf is  
 362 now effectively deeper.

363 2) THE CROSS-SHELFBREAK OUTFLOW OF SHELF WATER

364 The supply jet flow turns and crosses isobaths once it nears the eddy. The kinematic bottom  
 365 boundary condition  $w = u \cdot \nabla H$  requires that near-bottom water parcels in a cross-isobath flow move  
 366 vertically, advect the background density field and thereby create near-bottom density anomalies.  
 367 We now examine whether these density anomalies affect the vertical structure of the supply jet  
 368 when it turns to cross the shelfbreak. At the bottom, the *inviscid* density equation (5) can be written  
 369 in terms of buoyancy anomaly  $b = -g\rho/\rho_0$

$$\frac{Db}{Dt} + wN^2 = 0, \quad z = -H(y). \quad (14)$$

370 Assuming a steady outflow and applying the bottom boundary condition  $w = \mathbf{u} \cdot \nabla H$  yields

$$ub_x + vb_y = -(\mathbf{u} \cdot \nabla H)N^2, \quad z = -H(y); \quad (15)$$

371 Through thermal wind balance, the density anomaly can be expressed as geostrophic vertically-  
 372 sheared anomalous along- and cross-isobath velocity fields<sup>7</sup> ( $u^g, v^g$ ):  $f_0 v_z^g = b_x$  and  $-f_0 u_z^g = b_y$ .  
 373 Following Brink (1998), we write the LHS of (15) in vector form using  $\mathbf{u} = (u, v)$  and  $\mathbf{u}_z^g = (u_z^g, v_z^g)$ :

$$f_0 \mathbf{k} \cdot \mathbf{u} \times \mathbf{u}_z^g = -(\mathbf{u} \cdot \nabla H)N^2, \quad z = -H(y); \quad (16)$$

374 and then rewrite the above as

$$|\mathbf{u}| |\mathbf{u}_z^g| \sin \theta^z = -\frac{N^2}{f_0} |\mathbf{u}| |\nabla H| \cos \theta^H, \quad z = -H(y). \quad (17)$$

375  $\theta^z, \theta^H$  are the angles between the velocity vector  $\mathbf{u}$  and the geostrophic velocity shear vector  $\mathbf{u}_z^g$ ; and  
 376 between the velocity vector  $\mathbf{u}$  and the topographic gradient vector  $\nabla H$ . For non-zero cross-isobath  
 377 velocity (RHS  $\neq 0$ ), the LHS of (17) implies that

- 378 1. there must be near-bottom geostrophic shear ( $|\mathbf{u}_z^g| \neq 0$ ), and

---

<sup>7</sup>superscript  $g$  for geostrophy

379 2. this shear must necessarily be oriented at an angle to the velocity vector so that  $\sin \theta^H \neq 0$ , i.e.

380 acting to turn the jet.

381 We can now judge the effectiveness of the near-bottom geostrophic shear  $|\mathbf{u}_z^g|$  throughout the water

382 column by scaling (17). Using our previous assumption that the along-shelf supply jet velocity  $|\mathbf{u}|$

383 scales like the eddy velocity scale  $V_0$  and using  $L_\beta$  from (12),

$$\frac{|\mathbf{u}_z^g| H_{\text{sb}}}{|\mathbf{u}|} = \frac{\alpha_{\text{sh}} N^2 H_{\text{sb}}}{f_0 |\mathbf{u}|} \\ = \mathcal{O}\left(\frac{\alpha_{\text{sh}} N^2 H_{\text{sb}}}{f_0 V_0}\right) = \mathcal{O}\left(\frac{H_{\text{sb}}^2}{f^2 L_\beta^2 / N^2}\right) = \mathcal{O}(\varphi_o). \quad (18)$$

384 The modification of vertical shear by these near-bottom anomalies is of the same order as the

385 shear that would be present in a balanced jet of scale  $L_\beta$ , if the shelf is deep enough. Following

386 (18),  $\varphi_o$  should be an effective predictor of the shear of the cross-shelfbreak flow, just as for the

387 along-shelf supply jet. We check this prediction by calculating BC using the cross-shelf velocity  $v$

388 at the shelfbreak and testing its variation against  $\varphi_o$  (Figure 9d). Again, there is an approximately

389 linear dependence with  $\varphi_o$ . The offshore outflow of shelf water is increasingly vertically sheared as

390  $\varphi_o$  increases, as for the supply jet. Figure 9d presents a more nuanced, and more accurate, picture

391 than the average profiles in Figure 9a. The averaged profiles are colored such that darker gray lines

392 correspond to larger values of  $\varphi_o$ <sup>8</sup>. What appears to be a sharp change in vertical structure of the

393 offshore flow based on parameter  $\varphi_o$  in Figure 9a is actually a gradual linear increase of vertical

394 shear with  $\varphi_o$  in Figure 9d. The parameter BC in Figure 9d is a more accurate characterization of

395 the instantaneous state of the flow, whereas Figure 9a averages over the spatially complex dye field

396 at the shelfbreak (Figure 6b). Regardless, both diagnostics indicate that the eddy-forced offshore

397 flow samples the entire water column over the outer shelf ( $BC < 1$  throughout).

---

<sup>8</sup>the red lines illustrate that  $\varphi_o$  rather than  $\lambda$  controls the vertical structure of the offshore transport (Section 5a)

## 399 1) THE CROSS-SHELFBREAK INFLOW OF EDDY- AND SLOPE-WATERS

400 The vertical structure of the eddy water inflow onto the shelf is always baroclinic (Figure 9b).  
 401 The density anomaly-based reasoning of the previous section does not apply in this case because  
 402 the appropriate bottom slope, that of the continental slope, is quite steep ( $S_{\text{sl}} \geq 1$ , Table 2). The  
 403 kinematic bottom boundary condition imposes  $w = u \cdot \nabla H = \alpha v$  at the bottom,  $v$  being cross-isobath  
 404 velocity and  $\alpha$  bottom slope. For infinite slope  $\alpha$ , i.e. a vertical wall, the appropriate boundary  
 405 condition is  $v = 0$ . As bottom slope  $\alpha$  increases, there must be a transition from a regime where the  
 406 appropriate boundary condition is  $w = \alpha v$  to one where  $v = 0$ , i.e. as  $\alpha \rightarrow \infty$ ,  $v \rightarrow 0$  so that  $w$  is  
 407 bounded. The upper bound on  $w$  is set by the continuity equation which imposes  $w \leq O(VD/L)$ ,  
 408 where  $V$  is the cross-isobath velocity scale and  $D, L$  are appropriate vertical and horizontal scales.

409 Scaling  $w$  from the bottom boundary condition as  $w \sim O(\alpha_{\text{sl}} V)$  and comparing it to the upper  
 410 bound from the continuity equation  $O(VD/L)$  yields (assuming that  $D/L \sim f/N$ )

$$w \sim O(\alpha_{\text{sl}} V) \lesssim O(VD/L) \quad (19)$$

$$O(\alpha_{\text{sl}} V) \lesssim O(Vf/N) \Rightarrow S_{\text{sl}} \lesssim O(1). \quad (20)$$

411 When  $S_{\text{sl}} \lesssim O(1)$ , the slope is gentle and the cross-isobath flow is deflected either up- or down-slope  
 412 i.e.  $v_y \approx -w_z$  and the flow is approximately two-dimensional in the  $y - z$  plane. When  $S_{\text{sl}} > O(1)$ ,  
 413 the slope is steep and acts like a vertical wall that deflects the near-bottom cross-isobath flow in the  
 414 along-isobath direction. Now the flow is approximately two-dimensional in the horizontal  $x$ - $y$  plane  
 415 and  $u_x \approx -v_y$ .

416 Over the shelf where  $S_{\text{sh}} \leq 0.2$ , (19) is satisfied and the sloping shelf forces vertical motion affecting  
417 the supply jet as described in the previous section. For the continental slope however,  $S_{\text{sl}} \geq 1$  and the  
418 slope is expected to force  $v \approx 0$  as in Figure 11c. The thick green contour is for a tenth of the peak  
419 surface cross-isobath velocity. At the surface, the eddy forces a small but non-zero cross-isobath  
420 velocity  $v$ . Below shelfbreak depth, the slope forces  $v \approx 0$  and creates a stagnation line over the  
421 upper slope near the shelfbreak (Figure 11b), pinching the cross-shelf velocity contours in Figure  
422 11c. Near the surface there is still small but *non-zero* cross-shelfbreak flow forced by the eddy,  
423 resulting in strong vertical shear between the surface and shelfbreak depth (Figure 9b).

## 424 2) ALONG-SHELF FLOW OF EDDY- AND SLOPE-WATERS (THE LEAKAGE)

425 The baroclinic inflow of eddy and slope waters rotates to follow isobaths after it crosses the  
426 shelfbreak. Being strongly sheared at the shelfbreak (Figure 6c,d), we *hypothesize* that the  
427 cross-isobath scale of the balanced along-shelf flow should scale with the shelf deformation  
428 radius,  $NH_{\text{sb}}/f$ . This hypothesis is tested using the depth and time-averaged cross-shelf dye field  
429  $C_{\text{mean}}(y) = \text{mean}_{z,t} C(x_0, y, z, t)$  at a location  $x = x_0$  near the eastern sponge. The time-average is  
430 calculated over  $[t_{\text{start}}, t_{\text{stop}}]$ . The width of the eddy- and slope-water leakage on the shelf is defined  
431 as the  $y$ -location where  $C_{\text{mean}}(y) = Y_{\text{sb}}$ , this being the time- and depth-averaged location of the dye  
432 front between shelf and non-shelf waters. The instantaneous dye front is the thick blue contour  
433 in Figure 6c,d. The diagnosed location of the dye front scales linearly with the shelf deformation  
434 radius in Figure 10b, confirming our hypothesis.

435 **6. The cross-shelfbreak flux of shelf-water**

436 The addition of a sloping shelf reduces the cross-shelfbreak offshore transport of shelf water as  
437 compared to the corresponding flat shelf simulation (Section 4d). The effect of a shelf-slope is to  
438 reduce the volume of shelf water that can be affected by the eddy — the supply jet’s cross-shelf  
439 scale is reduced to  $1.22L_\beta$  (Section 5b). In contrast, the supply jet’s cross-shelf scale over a flat  
440 shelf is the forcing scale, i.e. an eddy radius, unless the shelf is narrower. For example, in Figure  
441 7 the shelf width is smaller than the eddy radius and the supply jet is visible over the entire shelf.  
442 We hypothesize that the reduction in the supply jet’s cross-shelf scale is the cause of the reduced  
443 offshore transport of shelf water, and will now test this assertion.

444 We make five assumptions.

- 445 1. First, for simplicity, assume that the eddy’s velocity field decays as an exponential function  
446 over the shelf in the *cross-shelf* direction.
- 447 2. Over a flat shelf, the decay scale for the exponential is the eddy’s horizontal scale  $L_0$ . Over a  
448 sloping shelf, we *assume* the cross-shelf decay scale to be  $L_s \equiv 1.22L_\beta$  instead of the eddy  
449 radius  $L_0$  (Figure 10a).
- 450 3. We assume that the eddy’s vertical scale is large compared to shelfbreak depth  $H_{\text{sb}}$ , so that the  
451 velocity field is barotropic.
- 452 4. We ignore the near-shelfbreak presence of eddy- and slope-waters.
- 453 5. Finally, we write the along-shelf velocity magnitude of shelf water in the supply jet as  $c_1V_0$ ,  
454 where  $V_0$  is the eddy velocity scale and  $c_1$  is an  $O(1)$  constant.

<sup>455</sup> The supply jet transport  $Q_f$  over a flat shelf of width  $L_{\text{sh}}$  is then the integral of the velocity field  
<sup>456</sup> ( $y \equiv y - Y_{\text{sb}}$  so that  $y = 0$  at the shelfbreak here)

$$Q_f = c_1 \int_{-L_{\text{sh}}}^0 \int_{-H_{\text{sb}}}^0 V_0 e^{-|y|/L_0} dz dy \quad (21)$$

$$= -c_1 V_0 H_{\text{sb}} L_0 \left[ 1 - e^{-(L_{\text{sh}}/L_0)} \right] \quad (22)$$

<sup>457</sup> Using  $L_s \equiv 1.22L_\beta$  instead of eddy radius  $L_0$  as the cross-shelf decay scale for the velocity field  
<sup>458</sup> over a sloping shelf, we analogously write

$$Q_\alpha = c_1 \int_{-L_{\text{sh}}}^0 \int_{-h(y)}^0 V_0 e^{-|y|/L_s} dz dy \quad (23)$$

$$= -c_1 V_0 H_{\text{sb}} L_s \left[ \left( 1 - \frac{\alpha_{\text{sh}} L_s}{H_{\text{sb}}} \right) \left( 1 - e^{-L_{\text{sh}}/L_s} \right) - \frac{\alpha_{\text{sh}} L_{\text{sh}}}{H_{\text{sb}}} e^{-L_{\text{sh}}/L_s} \right] \quad (24)$$

<sup>459</sup> We hypothesize that the effect of a sloping shelf is fully encapsulated in “slope factor”  $\sigma =$   
<sup>460</sup>  $Q_\alpha/Q_f, \alpha_{\text{sh}} \neq 0$  such that  $\sigma = 1$  when  $\alpha_{\text{sh}} = 0$ . We test this hypothesis by using four sets of  
<sup>461</sup> simulations<sup>9</sup>; each set is marked using a different marker in Figure 12. Within each set of simulations  
<sup>462</sup> (same markers), only the shelf-slope is changed. Between different sets (different markers),  
<sup>463</sup> both eddy and shelf properties are changed. We normalize the “true” average flux estimated for  
<sup>464</sup> simulations with a sloping shelf  $\widetilde{Q}_\alpha$  by the “true” average estimated for the corresponding flat  
<sup>465</sup> bottom run  $\widetilde{Q}_f$ . The ratio  $\widetilde{Q}_\alpha/\widetilde{Q}_f$  is well modeled by the straight line (Figure 12),

$$\frac{\widetilde{Q}_\alpha}{\widetilde{Q}_f} = 0.7\sigma + 0.3. \quad (25)$$

<sup>466</sup> A sloping shelf reduces the cross-shelf scale of the eddy’s influence, and in doing so, reduces the  
<sup>467</sup> offshore transport of shelf water.

<sup>468</sup> Cherian and Brink (2016, their Sections 8, 9d) regressed the true value of average offshore transport  
<sup>469</sup>  $\widetilde{Q}_\alpha$  for a sloping shelf against  $Q_f$  (prediction for flat shelf, their  $Q$ ) to obtain a offshore flux estimate

---

<sup>9</sup>The sets are {8380,8381, 8383, 8384, 8385}; {34, 8341}; {8350-2, 8351-2, 8352-2} and {8040, 8041, 8042} in Table 2.

470 for sloping shelves. Having proposed an explanation for how a sloping shelf influences offshore  
471 transport, we can easily update that recipe to use a decay scale of  $1.22L_\beta$  instead of the eddy radius  
472  $L_0$  when the shelf is sloping and obtain a better estimate of eddy-forced offshore flux of shelf  
473 water. Regressing the true value of average offshore transport  $\widetilde{Q}_\alpha$  against our updated prediction  
474  $Q_\alpha$  yields a regression slope of 0.2 and a correlation coefficient of 0.95. To summarize, in the case  
475 of a sloping shelf we calculate  $Q_\alpha$  using (24) after setting  $c_1 = 0.2$  to obtain an estimate of the  
476 eddy-forced offshore transport of shelf-water.

## 477 7. The effect of bottom friction

478 With the addition of bottom friction, the picture remains qualitatively similar. The presence of  
479 friction is more important than its magnitude, as is now described. We use a set of simulations  
480 where only *linear* bottom friction magnitude  $r_f$  is varied. Other parameters are set so that they  
481 match (nondimensionally) the interaction of Gulf Stream warm-core rings with the Middle Atlantic  
482 Bight. Compare an simulation with no bottom stress (Figure 13a,b) with one where linear bottom  
483 friction coefficient  $r_f = 3 \times 10^{-3} \text{ m s}^{-1}$ ,  $f_0 = 5 \times 10^{-5} \text{ s}^{-1}$ ,  $H_{\text{sb}} = 50 \text{ m}$  and Ekman number  $\text{Ek} =$   
484  $r_f/(f_0 H_{\text{sb}}) = 1.2$  (Figure 13c,d). Representative values for the real-world coastal ocean are  
485  $r_f = 5 \times 10^{-4} \text{ m s}^{-1}$  and  $\text{Ek} = 0.05$  for the Middle Atlantic Bight ( $f_0 = 10^{-4} \text{ s}^{-1}$  and  $H_{\text{sb}} = 100 \text{ m}$ ).  
486 Despite the large value, the flow evolution on the shelf is relatively unaffected (Figure 13a). All  
487 differences in the frictional simulation can be traced to the spin up of a stronger secondary cyclone  
488 that pulls the eddy away from the shelfbreak ( $x \approx 250\text{--}300 \text{ km}$  in Figure 13c,d; Cherian and Brink  
489 2016). The increased vorticity is generated in the bottom boundary layer over the slope. Both  
490 simulations are nearly identical till the eddy is pulled away, after which the forcing at the shel fbreak  
491 and over the shelf drops. There is a corresponding drop in cross-shelfbreak flux magnitude (Figure

8a) and the along-shelf flow over the shelf weakens (Figure 13d). This drop in flux magnitude at  
492  $t \approx 200$  days is similar to that seen for a frictional flat shelf (Figure 8a). When the shelf is sloping,  
493 frictional simulations attain nearly the same maximum flux as the corresponding inviscid simulation  
494 (compare blue lines in Figure 8a). The time averaged flux magnitude is lower because the eddy  
495 moves away from the shelfbreak frequently. Increasing  $r_f$  from  $5 \times 10^{-4} \text{ m s}^{-1}$  by a factor of six to  
496  $3 \times 10^{-3} \text{ m s}^{-1}$  does not change the flux magnitude time series; this insensitivity is surprising.  
497

498 The cross-shelf extent of the supply jet is also insensitive to bottom friction magnitude. For  
499 this section, we define the jet's cross-shelf extent as the cross-shelf distance over which the  
500 *instantaneous* along-shelf depth-averaged velocity drops to 30% of its value at the shelfbreak. The  
501 scale is estimated near the eastern boundary, downstream from the eddy. Time series of this quantity  
502 for simulations with  $r_f$  varying from  $0$ – $3 \times 10^{-3} \text{ m s}^{-1}$  are shown in Figure 13e. The reduction  
503 in cross-isobath scale at  $t \approx 230$  days occurs when the eddy is pulled away from the shelfbreak,  
504 reducing the forcing magnitude. Then the only significant shelf water velocities are near the leakage  
505 at the shelfbreak, where the along-shelf flow balances the density gradient between the ambient  
506 shelf water and the eddy water at the shelf-edge (Figure 13d). These conditions persist till the eddy  
507 loops back to the shelfbreak at  $t \approx 300$ – $320$  days, at which point there is significant eddy forcing  
508 over the shelf and  $BC(t)$  drops to approximately 0.1 indicating the presence of a barotropic supply  
509 jet. In total, varying non-zero bottom friction has *little effect* on the maximum cross-isobath extent  
510 of the supply jet despite the large variation in  $r_f$  values used. This conclusion is also supported by  
511  $C_{\min}(t)$  in Figure 8b.

512 Bottom friction could affect the scales of the along-isobath supply jet in three ways.

- 513 1. Buoyancy arrest might limit the jet's cross-isobath extent (Brink 2012),

514     2. If large enough, friction could modify the change the scale of the supply jet by changing the  
515       RHS of (11).

516     3. Arrested topographic wave physics could widen the jet downstream of the eddy (Csanady  
517       1978).

518     4. Stratified spindown might make the jet more baroclinic (Holton 1965).

519     Buoyancy arrest is easily ruled out: for barotropic flows, the expressions of Brink (2012) predict  
520       an along-isobath adjustment scale of at least a 1000 km for buoyancy arrest to influence the cross-  
521       isobath scale of the supply jet. Next, Section 5b argues that the cross-shelf scale of the supply jet is  
522       set by a relative vorticity constraint operating where the eddy forces the jet to turn offshore. We  
523       compare the stretching and frictional terms in (11) setting  $\alpha_{\text{sh}} = 10^{-3}$ ,  $L_\beta = 12 \text{ km}$  and  $H_{\text{sb}} = 50 \text{ m}$ ,

$$\frac{r_f u_y^{\text{bot}}}{f \alpha_{\text{sh}} v^{\text{bot}}} \sim O\left(\frac{r_f}{f_0 \alpha_{\text{sh}} L_\beta} \frac{u^{\text{bot}}}{v^{\text{bot}}}\right) \quad (26)$$

$$\sim \frac{Ek}{O(10^{-3} \times 12 \times 10^3 / 50)} \times O(u/v) \approx 4 Ek \times O(u^{\text{bot}} / v^{\text{bot}}). \quad (27)$$

524     Where the jet turns offshore near the eddy,  $u^{\text{bot}} \sim v^{\text{bot}}$  and friction is as important as the stretching  
525       term when  $Ek \geq 0.25$ . By generating anticyclonic vorticity and thence reducing the RHS, it should  
526       widen the supply jet. Instead, the supply jet's cross-isobath scale is relatively unmodified from its  
527       inviscid value for  $Ek = 0.02, 0.04, 0.2, 1.2$  ( $t < 230$  days in Figure 13e). We have not been able to  
528       rationalize this insensitivity but note that the frictional term is much smaller than the stretching term  
529       in (11) for the realistic value  $Ek \sim 0.05$  and  $L_\beta$  is expected to be a good estimate of the supply jet's  
530       cross-shelf scale. In some contexts the insensitivity to large values of bottom friction indicates that  
531       stratified spindown has reduced near-bottom velocities so that the frictional term is less important

532 (for e.g. Brink 2017). However, we now show that stratified spindown too is ineffective and that the  
533 supply jet is nearly-barotropic.

534 At first, it appears that bottom friction does make the along-shelf supply jet more baroclinic, as  
535 measured by the *time series*  $BC(t)$  (Figure 13f). The time series is obtained using (9) at each time  
536 step; i.e. we do *not* compute the median over  $[t_{\text{start}}, t_{\text{stop}}]$  in this case. As with the reduction in  
537 cross-isobath scale, the localized along-shelf baroclinic flow of the leakage is responsible for the  
538 much larger value of  $BC(t)$  at  $t = 230$  days. Prior to this time, the evolution of  $BC(t)$  is comparable  
539 to that of the inviscid simulation. When there is substantial eddy forcing over the shelf, frictional  
540 and inviscid simulations are near-identical. The explanation is that stratified spindown is expected  
541 to act over a vertical scale  $\sim O(fL/N)$ . For this particular simulation, the jet is barotropic with  
542 approximate cross-isobath scale  $L_\beta = \sqrt{V_0/\beta_{\text{sh}}}$ . Its vertical scale  $fL_\beta/N \approx 4H_{\text{sb}}$ , i.e.  $\varphi_o = 0.06^{10}$ ,  
543 so the spin-down should affect the water column equally at all depths above the bottom Ekman  
544 layer. BC, being calculated over the shelf above the bottom Ekman layer, is thus unaffected by the  
545 spin-down (Figure 13f). Vertical profiles of the outflow at the shelfbreak are also barotropic with a  
546 shallow Ekman layer near the bottom (Figure 8c). In addition, the bottom stress over the shelf does  
547 increase with increasing bottom friction parameter  $r_f$  indicating that spindown is not occurring.

548 One can also rule out arrested topographic wave physics (Csanady 1978). For a *linear* flow, the  
549 balance in (11) reduces to one between near-bottom vortex stretching and frictional spindown:

$$0 = \beta_{\text{sh}} v^{\text{bot}} - \frac{r_f}{H} \zeta^{\text{bot}}. \quad (28)$$

550 Csanady (1978) shows this equation to be diffusive: the along-shelf flow spreads (diffuses) in the  
551 cross-shore direction, becoming wider or narrower as it moves in the coastal-trapped wave direction.  
552 The flow must cross isobaths and generate stretching or compression to compensate for frictional

---

<sup>10</sup>just as for Gulf-Stream warm-core rings at the Middle Atlantic Bight

removal of vorticity<sup>11</sup>. If such a balance were possible, the along-shelf supply jet in Figure 13c,d would widen as it approaches the eastern boundary, changing the volume of shelf water affected by the eddy. Near the eastern boundary, the along-shelf scale of the supply jet is much larger than its cross-shore scale (Figure 13c) and accordingly cross-sections show that  $u^{\text{bot}} \sim O(100)v^{\text{bot}}$ . Equation (26) then implies that these scales are such that the flow cannot generate enough vorticity through near-bottom stretching to compensate for frictional spindown. The *steady-state* arrested topographic wave balance in (28) cannot be realized and the supply jet’s width is unchanged as it propagates downstream.

In summary, all differences in the frictional simulations can be traced to the spinup of a stronger secondary cyclone when the eddy impacts the continental slope. The cross-shelf scale of the supply jet is insensitive to the magnitude of friction. A dynamical explanation for this behaviour remains elusive. Bottom friction on the continental *slope* has a greater effect on the eddy-shelf interaction than bottom friction on the shelf.

## 8. Discussion

### a. Summary

We used a suite of continuously stratified primitive equation simulations to study the interaction of anticyclonic eddies with continental shelf-slope topography. Cherian and Brink (2016) described the fate of the exported shelf water and proposed a scaling for the magnitude of offshore flux of shelf water for a flat shelf. Here, we studied the shelf flows forced by these eddies and derived

---

<sup>11</sup>Csanady’s version is recovered for a barotropic flow with SSH  $\eta(x,y,t)$  by setting  $v^{\text{bot}} = g/f\eta_x$ ,  $\zeta^{\text{bot}} = g\nabla^2\eta$  and making the long wave assumption —  $L_x \gg L_y$ ,  $v^{\text{bot}}/u^{\text{bot}} \sim L_y/L_x \ll 1$  — so that  $\zeta^{\text{bot}} \approx g\eta_{yy}$ .

scalings for their horizontal and vertical structure (summarized in Figure 4). These scalings allowed us to extend the offshore flux parameterization of Cherian and Brink (2016) to account for a sloping shelf. The broad conclusions presented in Cherian and Brink (2016) regarding volume budgets for the Mid-Atlantic Bight shelf are unchanged.

The shelf water exported by the eddy never returns to the shelf: it is trapped in the stacked cyclones described in Cherian and Brink (2016) (also, Figure 2). The lost shelf water is compensated by an along-shelf jet that supplies shelf water from downstream of the eddy, in the coastal-trapped or Kelvin wave sense, as in the linear simulations of Chapman and Brink (1987) and as speculated by Lee and Brink (2010). This along-shelf supply jet is barotropic and its cross-shelf scale is limited: distance  $1.22L_\beta = 1.22\sqrt{V_0/\beta_{sh}}$  from the shelfbreak on average (Figure 4, 7 and 10).  $L_\beta$  can be interpreted as either a turning radius, an inertial length scale or a stationary topographic Rossby wave length scale (Pedlosky 1987). For the presented simulations, the supply jet is generally barotropic and its vertical shear depends on parameter  $\varphi_o$ , a Burger number comparing the jet's cross-shelf scale  $L_\beta$  to the shelf Rossby radius. On nearing the eddy, the along-shelf supply jet turns offshore. The near-bottom density anomalies created when the jet turns, and crosses isobaths, are generally not strong enough to appreciably change the vertical structure of the jet (Figure 9).

The eddy also transports eddy and slope waters on to the shelf, compensating for the lost shelf water volume. These waters form a gravity current-like flow moving downstream in the Kelvin-wave direction, whose average cross-shelf extent is a shelf Rossby radius from the shelfbreak (also see Shi and Nof 1993; Zhang and Gawarkiewicz 2015). The baroclinic nature of the current is apparent in cross-shelf sections of the flow field (Figure 6c,d). Most notably, the vertical structure of the shelf water outflow and eddy water inflow can be different. At the shelf edge, the offshore flow of shelf water is generally barotropic (vertically uniform) while the onshore flow of eddy- and slope-waters

595 is generally baroclinic (vertically sheared, Figures 9). Qualitatively, linear bottom friction has little  
 596 effect on the shelf flow field. Its biggest effect is to strengthen the secondary cyclone that pulls the  
 597 eddy away from the shelfbreak; thereby reducing the strength of the eddy forcing on average. The  
 598 above results are subject to the same caveat as Cherian and Brink (2016) i.e. the planetary  $\beta$ -plane  
 599 continuously forces the eddy into the slope. Without competing influences from background flows  
 600 and other mesoscale eddies, the eddy's edge always reaches the shelfbreak, remains there for a large  
 601 amount of time and strongly affects the shelf. Our scalings for length scales and cross-shelf fluxes  
 602 are thus an upper bound. With this in mind, we now discuss implications for the Mid-Atlantic  
 603 Bight.

604 *b. Implications and observations: the Mid-Atlantic Bight shelf*

605 For the Mid-Atlantic Bight shelf,  $\alpha_{\text{sh}} \approx 10^{-3} \text{ m m}^{-1}$ , annual mean  $N \approx 10^{-2} \text{ s}^{-1}$  (Zhang et al. 2011),  
 606  $f_0 = 10^{-4} \text{ s}^{-1}$  and  $H_{\text{sb}} \approx 100 \text{ m}$ . A typical Gulf Stream warm-core ring velocity is  $O(1.5 \text{ m s}^{-1})$ .  
 607 Using these values, the Burger number

$$\varphi_o = \frac{S_{\text{sh}}NH_{\text{sb}}}{V_0} = \frac{0.1 \times 10^{-2} \times 100}{1.5} \approx 0.06. \quad (29)$$

608 The estimated  $\varphi_o$  suggests that shelf water outflow should be barotropic above the bottom boundary  
 609 layer and that the along-shelf supply jet width should scale like  $1.22L_\beta$ . With the above choices,  
 610 warm-core rings should be able to extract shelf water parcels that are an approximate distance  
 611 of  $1.22L_\beta \approx 55 \text{ km}$  from the shelfbreak. The eddy water inflow is expected to penetrate about  
 612  $1.33NH_{\text{sb}}/f_0 \approx 14 \text{ km}$  inshore. We remind the reader that these length scale estimates are an  
 613 (average) upper bound. Bottom friction should not affect these estimates which are based on an  
 614 inviscid theory (Section 7).

615 Drifter observations reported in Brink et al. (2003) indicate that shelf water between the surface  
616 and at least 40 m depth<sup>12</sup> are exported by warm-core rings at the shelfbreak off George's Bank  
617 (shelfbreak depth 100 m; Figure 1). The most onshore drifter that crossed the shelfbreak started at  
618 the 60 m isobath, roughly 50 km inshore of the shelfbreak, consistent with our prediction of 60 km.  
619 Lee and Brink (2010) too observed that the ring affected the entire shelf water column from surface  
620 to bottom (less than 100 m deep here). Their observations show the warm eddy water intrusion  
621 (leakage) extends nearly to the shelf bottom in some places. The associated velocity field was  
622 surface intensified "with little or no flow near the bottom". The latter is again as expected since  
623  $S_{sl} > 1$  for the continental slope off the Mid-Atlantic Bight (Figure 9b and Section 5c2). Ring water  
624 is present roughly 25–40 km inshore of the 100 m isobath, much larger than our estimate of 14 km.  
625 Sections presented in Lee and Brink (2010) do show the enhanced penetration to be associated with  
626 the eddy water intrusion wrapping up into a small eddy approximately 20 km wide. Such processes  
627 are not accounted for in our prediction of the *average* cross-shelf scale. More recently, Zhang and  
628 Gawarkiewicz (2015) observed warm-core ring water intruding approximately 20 km inshore of  
629 the 100 m isobath, better agreement with our 14 km estimate. Glider observations in Zhang and  
630 Gawarkiewicz (2015) too show ring density water extending nearly to the bottom just as in Figure  
631 6d and Lee and Brink (2010). These observations are generally consistent with the predictions  
632 presented previously despite the absence of a shelfbreak front in our simulations.

633 The updated parameterization that accounts for a sloping shelf yields the same shelf-water flux  
634 estimate for the Mid-Atlantic Bight presented in Cherian and Brink (2016, their Section 9d), viz.  
635 0.3–0.7 Sv. Since the conclusions are unchanged, the reader is referred there for a discussion of  
636 this flux estimate in the context of existing budgets for the Mid-Atlantic Bight shelf.

---

<sup>12</sup>no drifters were drogued below this depth

637 *c. Limitations and future extensions*

638 As in Cherian and Brink (2016), there are drawbacks to the approach used. One, in the absence of  
639 competing influences on the eddy’s trajectory, the  $\beta$ -plane continuously makes the eddy self-advect  
640 into the topography and the interaction is always severe. Further, the simulated eddies spend large  
641 amounts of time at the shelfbreak (hundreds of days). The trajectory of large eddies in the ocean is  
642 certainly influenced by the presence of ambient flow features. Real eddies need not continually be  
643 at the shelfbreak, unlike the presented simulations. Our scalings are likely over-estimates for this  
644 reason. It is necessary that these scalings be checked against long-term simulations that include  
645 additional variability similar to those of Stewart and Thompson (2015).

646 Two, there is no shelfbreak front in any of these simulations. Since the eddy has a much larger  
647 velocity signature than the shelfbreak jet associated with the front, we expect that predictions for the  
648 shelf water outflow are unaffected by the presence of a front. Accordingly, laboratory experiments  
649 by Cenedese et al. (2013) indicate that for such “strong interactions”, the shelf water is permanently  
650 exported and is sourced from inshore of the shelfbreak jet’s velocity maximum. At the Mid-Atlantic  
651 Bight, existing observations and simulations do indicate that the front moves inshore where the  
652 eddy forces an inflow (for e.g., Zhang and Gawarkiewicz 2015). The front appears not to prevent  
653 eddy water from crossing on to the shelf, so our results might be applicable at least when the eddy  
654 is at the shelfbreak. Once the eddy forcing has relaxed, the front should present a barrier to eddy  
655 water mixing in with shelf water. These assertions are very tentative and must be tested against  
656 high resolutions simulations involving a shelfbreak front, such as those reported by Zhang and  
657 Gawarkiewicz (2015).

658 Third, the onshore flux of eddy- and slope-waters has yet to be parameterized. Such a scaling is  
659 critical for assessing how important eddy-driven cross-shelf exchange is to closing the salt budget  
660 of Lentz (2010). Fourth, the apparent insensitivity of the supply jet's cross-shelf scale when bottom  
661 friction is varied significantly must be examined in more detail. Fifth, the simulations have ignored  
662 the effect of surface forcing as well as along-shelf topographic variations (e.g. canyons). Both  
663 might conceivably have an effect on flux magnitude and flow scales. Finally and perhaps most  
664 importantly, all predictions here must be tested against an extensive observational dataset. The  
665 eddy-shelf interaction problem still presents multiple intriguing challenges; ones that must be  
666 addressed with both high fidelity numerical models and high resolution observations.

667 *Acknowledgments.* This paper constitutes part of DAC's Ph.D. thesis. Both the thesis and this  
668 manuscript owe much to Steve Lentz's suggestions and many intriguing questions. Multiple  
669 stimulating discussions with Glenn Flierl and Amala Mahadevan are also gratefully acknowledged.  
670 We also thank two anonymous reviewers for kind and helpful feedback. We acknowledge high-  
671 performance computing support from Yellowstone (<http://n2t.net/ark:/85065/d7wd3xhc>)  
672 provided by NCAR's Computational and Information Systems Laboratory, sponsored by the  
673 National Science Foundation. We would like to acknowledge high-performance computing support  
674 from Cheyenne ([doi:10.5065/D6RX99HX](https://doi.org/10.5065/D6RX99HX)) provided by NCAR's Computational and Information  
675 Systems Laboratory, sponsored by the National Science Foundation. The research presented here  
676 was funded by the U.S. National Science Foundation's Physical Oceanography program through  
677 grants OCE-1059632 and OCE-1433953. Funding support from the Academic Programs Office,  
678 Woods Hole Oceanographic Institution is also gratefully acknowledged.

679    **References**

- 680    Beardsley, R. C., D. C. Chapman, K. H. Brink, S. R. Ramp, and R. J. Schlitz, 1985: The Nantucket  
681    Shoals Flux Experiment (NSFE79). Part I: A Basic Description of the Current and Temperature  
682    Variability. **15** (6), 713–748, doi:10.1175/1520-0485(1985)015<0713:TNSFEP>2.0.CO;2.
- 683    Beron-Vera, F. J., Y. Wang, M. J. Olascoaga, G. J. Goni, and G. Haller, 2013: Objective Detection  
684    of Oceanic Eddies and the Agulhas Leakage. **43** (7), 1426–1438, doi:10.1175/JPO-D-12-0171.1.
- 685    Brink, K. H., 1998: Deep Sea Forcing and Exchange Processes. *Sea*, K. H. Brink, and A. R.  
686    Robinson, Eds., Vol. 10, John Wiley & Sons, Inc., chap. 6, 151–167.
- 687    Brink, K. H., 2012: Buoyancy Arrest and Shelf–Ocean Exchange. **42** (4), 644–658, doi:10.1175/  
688    JPO-D-11-0143.1.
- 689    Brink, K. H., 2017: Surface Cooling, Winds, and Eddies over the Continental Shelf. *Journal of*  
690    *Physical Oceanography*, **47** (4), 879–894, doi:10.1175/JPO-D-16-0196.1.
- 691    Brink, K. H., R. Limeburner, and R. C. Beardsley, 2003: Properties of flow and pressure over  
692    Georges Bank as observed with near-surface drifters. **108** (C11), doi:10.1029/2001JC001019.
- 693    Burger, A. P., 1958: Scale Consideration of Planetary Motions of the Atmosphere. **10** (2), 195–205,  
694    doi:10.1111/j.2153-3490.1958.tb02005.x.
- 695    Cenedese, C., R. E. Todd, G. G. Gawarkiewicz, W. B. Owens, and A. Y. Shcherbina, 2013: Offshore  
696    Transport of Shelf Waters through Interaction of Vortices with a Shelfbreak Current. **43** (5),  
697    905–919, doi:10.1175/JPO-D-12-0150.1.
- 698    Chapman, D. C., 1985: Numerical treatment of cross-shelf open boundaries in a barotropic coastal  
699    ocean model. *J. Phys. Oceanogr.*, **15** (8), 1060–1075.

- 700 Chapman, D. C., and K. H. Brink, 1987: Shelf and slope circulation induced by fluctuating offshore  
701 forcing. **92** (C11), 11 741, doi:10.1029/JC092iC11p11741.
- 702 Chelton, D. B., M. G. Schlax, and R. M. Samelson, 2011: Global observations of nonlinear  
703 mesoscale eddies. **91** (2), 167–216, doi:10.1016/j.pocean.2011.01.002.
- 704 Cherian, D. A., 2016: When an eddy encounters shelf-slope topography. Ph.D. thesis, 135 pp.
- 705 Cherian, D. A., and K. H. Brink, 2016: Offshore transport of shelf water by deep-ocean eddies.  
706 **46** (12), 3599–3621, doi:10.1175/JPO-D-16-0085.1.
- 707 Csanady, G. T., 1978: The Arrested Topographic Wave. **8** (1), 47–62, doi:10.1175/1520-0485(1978)  
708 008<0047:TATW>2.0.CO;2.
- 709 Early, J. J., R. M. Samelson, and D. B. Chelton, 2011: The Evolution and Propagation of Quasi-  
710 geostrophic Ocean Eddies. **41** (8), 1535–1555, doi:10.1175/2011JPO4601.1.
- 711 Flierl, G. R., M. E. Stern, and J. A. Whitehead, 1983: The physical significance of modons: Labo-  
712 ratory experiments and general integral constraints. **7** (4), 233–263, doi:10.1016/0377-0265(83)  
713 90007-6.
- 714 Holton, J. R., 1965: The influence of Viscous Boundary Layers on Transient Motions in a Stratified  
715 Rotating Fluid. Part I. **22** (4), 402–411, doi:10.1175/1520-0469(1965)022<0402:TIOVBL>2.0.  
716 CO;2.
- 717 Joyce, T. M., J. K. Bishop, and O. B. Brown, 1992: Observations of offshore shelf-water transport  
718 induced by a warm-core ring. **39**, S97–S113, doi:10.1016/S0198-0149(11)80007-5.
- 719 Lee, C. M., and K. H. Brink, 2010: Observations of storm-induced mixing and Gulf Stream Ring  
720 incursion over the southern flank of Georges Bank: Winter and summer 1997. **115** (C8), 1–19,  
721 doi:10.1029/2009JC005706.

- 722 Lentz, S. J., 2010: The Mean Along-Isobath Heat and Salt Balances over the Middle Atlantic Bight  
723      Continental Shelf. **40** (5), 934–948, doi:10.1175/2009JPO4214.1.
- 724 Linder, C. A., and G. G. Gawarkiewicz, 1998: A climatology of the shelfbreak front in the Middle  
725      Atlantic Bight. **103** (C9), 18 405, doi:10.1029/98JC01438.
- 726 Marchesiello, P., J. C. McWilliams, and A. F. Shchepetkin, 2001: Open boundary conditions for  
727      long-term integration of regional oceanic models. **3** (1-2), 1–20, doi:10.1016/S1463-5003(00)  
728      00013-5.
- 729 Mason, E., M. J. Molemaker, A. F. Shchepetkin, F. Colas, J. C. McWilliams, and P. Sangrà, 2010:  
730      Procedures for offline grid nesting in regional ocean models. **35** (1-2), 1–15, doi:10.1016/j.  
731      ocemod.2010.05.007.
- 732 McWilliams, J. C., and G. R. Flierl, 1979: On the Evolution of Isolated, Nonlinear Vortices. **9** (6),  
733      1155–1182, doi:10.1175/1520-0485(1979)009<1155:OTEONI>2.0.CO;2.
- 734 Mied, R. P., and G. J. Lindemann, 1979: The Propagation and Evolution of Cyclonic Gulf Stream  
735      Rings. **9** (6), 1183–1206, doi:10.1175/1520-0485(1979)009<1183:TPAEOC>2.0.CO;2.
- 736 Myers, R. A., and K. Drinkwater, 1989: The influence of Gulf Stream warm core rings on recruit-  
737      ment of fish in the northwest Atlantic. **47** (3), 635–656, doi:10.1357/002224089785076208.
- 738 Nof, D., 1983: On the migration of isolated eddies with application to Gulf Stream rings. **41** (3),  
739      399–425, doi:10.1357/002224083788519687.
- 740 Oey, L.-Y., and H. Zhang, 2004: The generation of subsurface cyclones and jets through eddy–slope  
741      interaction. **24** (18), 2109–2131, doi:10.1016/j.csr.2004.07.007.

- 742 Okkonen, S. R., T. J. Weingartner, S. Danielson, D. Musgrave, and G. Schmidt, 2003: Satellite and  
743 hydrographic observations of eddy-induced shelf-slope exchange in the northwestern Gulf of  
744 Alaska. **108 (C2)**, 3033, doi:10.1029/2002JC001342.
- 745 Pedlosky, J., 1987: *Geophysical Fluid Dynamics*. 2nd ed., Springer study edition, Springer, New  
746 York, oCLC: 844111849.
- 747 Ramp, S. R., R. C. Beardsley, and R. Legeckis, 1983: An Observation of Frontal Wave Development  
748 on a Shelf-Slope/Warm Core Ring Front Near the Shelf Break South of New England. **13 (5)**,  
749 907–912, doi:10.1175/1520-0485(1983)013<0907:AOOFWD>2.0.CO;2.
- 750 Shchepetkin, A. F., and J. C. McWilliams, 2003: A method for computing horizontal pressure-  
751 gradient force in an oceanic model with a nonaligned vertical coordinate. **108 (C3)**, 3090,  
752 doi:10.1029/2001JC001047.
- 753 Shchepetkin, A. F., and J. C. McWilliams, 2005: The regional oceanic modeling system (ROMS):  
754 a split-explicit, free-surface, topography-following-coordinate oceanic model. **9 (4)**, 347–404,  
755 doi:10.1016/j.ocemod.2004.08.002.
- 756 Shi, C., and D. Nof, 1993: The splitting of eddies along boundaries. **51 (4)**, 771–795, doi:10.1357/  
757 0022240933223927.
- 758 Stewart, A. L., and A. F. Thompson, 2015: Eddy-mediated transport of warm Circumpolar Deep  
759 Water across the Antarctic Shelf Break. **42 (2)**, 432–440, doi:10.1002/2014GL062281.
- 760 Tranter, D. J., D. J. Carpenter, and G. S. Leech, 1986: The coastal enrichment effect of the East  
761 Australian Current eddy field. *Deep Sea Research Part A. Oceanographic Research Papers*,  
762 **33 (11)**, 1705 – 1728, doi:10.1016/0198-0149(86)90075-0.

- <sup>763</sup> Zhang, W. G., and G. G. Gawarkiewicz, 2015: Dynamics of the direct intrusion of Gulf Stream
- <sup>764</sup> ring water onto the Mid-Atlantic Bight shelf. **42 (18)**, 7687–7695, doi:10.1002/2015GL065530.
- <sup>765</sup> Zhang, W. G., G. G. Gawarkiewicz, D. J. McGillicuddy Jr., and J. L. Wilkin, 2011: Cli-
- <sup>766</sup> matological Mean Circulation at the New England Shelf Break. **41 (10)**, 1874–1893, doi:
- <sup>767</sup> 10.1175/2011JPO4604.1.

## 768 **List of Tables**

769	<b>Table 1.</b> Terminology used in this paper. . . . .	42
770	<b>Table 2.</b> Simulation parameters. . . . .	43

Table 1: Terminology used in this paper.

Term	Definition
$(L_0, L^z)$	Gaussian horizontal and vertical scales of the eddy
$(x_{\text{cen}}(t), y_{\text{cen}}(t))$	Location of the eddy's center (SSH maximum)
$V_0$	Maximum azimuthal velocity in eddy
$f_0$	Coriolis frequency
$Y_{\text{sb}}, H_{\text{sb}}$	Shelfbreak location and depth
$r_f$	Linear bottom drag coefficient ( $\text{m s}^{-1}$ )
$\lambda$	$H_{\text{sb}}/L^z$ , non-dimensional shelfbreak depth
$\alpha_{\text{sh}}, \alpha_{\text{sl}}$	Bottom slope magnitude on shelf and slope
$L_{\text{sh}}$	Shelf width
$S_{\text{sh}}, S_{\text{sl}}$	$\frac{\alpha N}{f}$ , Shelf and slope Burger numbers
$\text{Ro}$	$\frac{V_0}{f_0 L_0}$ , Rossby Number
$\text{Ek}$	Ekman number $r_f/(f_0 H_{\text{sb}})$
$\beta$	$\frac{df}{dy}$
$\beta_{\text{sh}}$	Topographic $\beta$ , $\frac{f_0}{H_{\text{sb}}} \alpha_{\text{sh}}$
$C, E$	Passive tracers: cross-shelf dye & eddy-water dye
$L_\beta$	$\sqrt{\frac{V_0}{\beta_{\text{sh}}}}$
$C_{\min}$	Minimum value of cross-shelf dye crossing the shelfbreak at time instant $t$
$C_{\text{mean}}(y)$	Time- and depth-averaged cross-shelf dye field at $y$ .
$(u^{\text{bot}}, v^{\text{bot}})$	Bottom velocity
$\zeta$	Relative vorticity
$\text{BC}$	Baroclinicity, a measure of vertical shear in flow velocity

Table 2: Simulation parameters.

	Rh	Ro	$\beta$ ( $10^{-10}$ m $^{-1}$ s $^{-1}$ )	$\beta_{\text{sh}}$ ( $10^{-10}$ m $^{-1}$ s $^{-1}$ )	$\phi_o$	$\lambda$	$S_{\text{sl}}$	$S_{\text{sh}}$	$L_\beta$ (km)	$L_{\text{def}}$ (km)	$r_f$ ( $10^{-4}$ m s $^{-1}$ )	$L_{\text{atw}}$ (km)
ew-04	3.06	0.10	0.60	0.00	0.00	0.20	1.50	0.00	0	4		
ew-8040	3.08	0.10	0.60	1.52	0.02	0.19	1.50	0.01	34	4		
ew-8041	3.09	0.10	0.60	7.83	0.08	0.19	1.50	0.05	12	4		
ew-8042	3.06	0.10	0.30	8.03	0.18	0.18	1.50	0.10	17	7		
ew-82342	7.34	0.10	0.10	1.92	0.64	0.54	1.00	0.10	21	16		
ew-82343	7.34	0.10	0.10	2.84	0.98	0.55	1.00	0.15	17	16		
ew-34	11.72	0.10	0.15	0.00	0.00	0.15	1.50	0.00	0	3		
ew-8341	13.19	0.11	0.15	7.83	0.08	0.14	1.50	0.05	12	3		
ew-8350-2	14.93	0.19	0.15	0.00	0.00	0.17	3.06	0.00	0	7		
ew-8351-2	14.93	0.19	0.15	2.25	0.10	0.17	3.06	0.05	23	7		
ew-8352-2	14.93	0.19	0.15	4.70	0.20	0.16	3.06	0.10	16	7		
ew-8352	17.23	0.15	0.035	1.82	0.22	0.28	1.00	0.10	24	11		
ew-8342-2	5.93	0.08	0.15	4.70	0.50	0.19	3.06	0.10	11	7		
ew-8380	18.90	0.16	0.050	0.00	0.00	0.22	1.00	0.00	0	9		
ew-8381	18.90	0.16	0.050	1.68	0.07	0.22	1.00	0.05	35	9		
ew-8384	18.90	0.17	0.050	5.02	0.22	0.22	1.00	0.15	20	9		
ew-8385	18.58	0.16	0.050	6.39	0.31	0.23	1.00	0.20	18	10		
ew-8383	13.44	0.12	0.050	3.28	0.51	0.37	1.00	0.15	20	14		
ew-8392	31.82	0.24	0.035	2.13	0.48	0.22	3.00	0.20	28	19		
ew-583411	13.19	0.11	0.15	7.83	0.05	0.15	1.50	0.05	12	3	30	21
ew-583413	13.19	0.11	0.15	7.83	0.05	0.15	1.50	0.05	12	3	5.0	123
ew-583414	13.19	0.11	0.15	7.83	0.05	0.15	1.50	0.05	12	3	1.0	617
ew-583415	13.19	0.11	0.15	7.83	0.05	0.15	1.50	0.05	12	3	0.50	1234

771 List of Figures

- |     |                |   |    |
|-----|----------------|---|----|
| 772 | <b>Fig. 1.</b> | In this modified AVHRR image from Johns Hopkins University Applied Physics Laboratory, a Gulf Stream warm-core ring transports a filament of shelf water offshore. Topographic contours are overlaid in gray (50, 80, 2000, 4000 and 5000-m isobaths). The solid black contour is the 100 m isobath, generally considered the shelfbreak. . . . .   | 46 |
| 776 | <b>Fig. 2.</b> | Snapshots of the cross-shelf dye field at the surface. Black contours are SSH, dashed contours indicate negative values. Thick white dashed lines mark the shelf- and slope-break. The evolution is just as in the flat shelf simulations of Cherian and Brink (2016). . . . .  | 47 |
| 779 | <b>Fig. 3.</b> | $x-t$ Hovmoeller diagram of depth-averaged cross-shelf velocity at the shelfbreak. Offshore flow is in red and onshore flow in blue. Solid and dashed lines respectively mark the eddy's center and its edges in the along-isobath direction. Both the offshore and onshore flow are largest near the eddy. The along-isobath scale of both the outflow and the inflow is approximately an eddy radius. Small scale anticyclones formed by the instability of the eddy water leakage propagate downstream in the coastal trapped wave direction. . . . .  | 48 |
| 783 | <b>Fig. 4.</b> | Schematic flowfield forced by a deep-water eddy at the shelfbreak. MAB stands for Middle-Atlantic Bight. . . . .  | 49 |
| 787 | <b>Fig. 5.</b> | Volume budget for the shelf: defined as a volume bounded by the two sponges, the coastal wall and the shelfbreak. The export across the shelfbreak is compensated by an along-shelf jet moving water from the open eastern boundary into the shelf-domain, as well as the onshore flow of eddy- and slope-waters. . . . .   | 50 |
| 791 | <b>Fig. 6.</b> | Instantaneous cross-sections at $t = 300$ days from the simulation in Figure 2. (a) $x-y$ section of cross-shelf dye at the surface. (b) $x-z$ section of cross-shelf velocity at the shelfbreak. (c, d) $y-z$ section of along-shore velocity at $x = 350$ km, downstream of the eddy. Note different $x$ -axis limits in panels (c) and (d). . . . .  | 51 |
| 795 | <b>Fig. 7.</b> | Horizontal velocity vectors and cross-shelf dye at the surface for a flat shelf and a sloping shelf simulation. With a flat shelf, all of the shelf is forced into motion to supply the offshore flow at the shelfbreak. With a sloping shelf, there is a limit to the extent of the eddy's influence on the shelf. . . . .   | 52 |
| 799 | <b>Fig. 8.</b> | Offshore flow at the shelfbreak is strongly influenced by a shelf slope and not much influenced by friction. The reddish lines are for a flat shelf, and the bluish lines are for a sloping shelf. Dashes and filled circles indicate frictional simulations. $S_{sh}$ is the slope Burger number for the shelf and $r_f$ , the linear bottom drag coefficient in m/s. (a) Time series of offshore flux at the shelfbreak. The two frictional simulations with a sloping shelf have a nearly identical flux time series. (b) Lowest value of cross-shelf dye crossing the shelfbreak at that instant; i.e., the extent to which the eddy can extract water off the shelf. Adding a slope reduces the cross-shelf scale while increasing friction with a slope does not change much. (c) Vertical structure of the $(x,t)$ -integrated offshore transport. . . . . | 53 |
| 803 | <b>Fig. 9.</b> | (a,b) Vertical profiles of the time-averaged shelf water outflow and non-shelf water inflow at the shelfbreak. The time average is over $[t_{start}, t_{stop}]$ . The thick black lines are for a simulation with a flat shelf, $\phi_o = 0$ and $S_{sl} = 1.5$ . The inflow is always baroclinic while the outflow is only sometimes baroclinic (Section 5). Values are normalized such that the maximum value in each profile is 1. (c,d) The shelf water supply jet is more baroclinic, as measured by $BC$ in equation (9), for larger values of non-dimensional parameter $\phi_o$ (Section 5b). Two   | 54 |



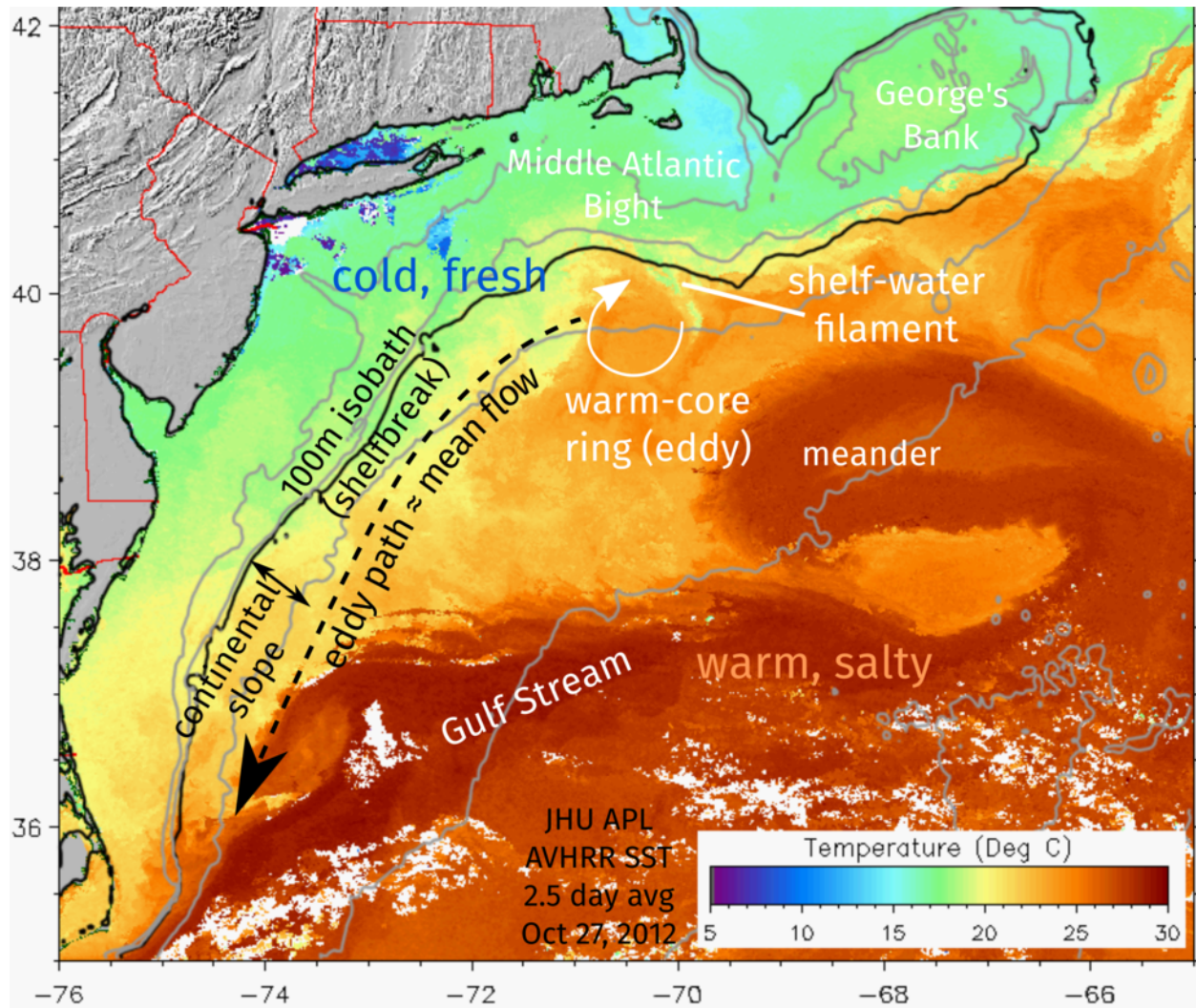


Figure 1: In this modified AVHRR image from Johns Hopkins University Applied Physics Laboratory, a Gulf Stream warm-core ring transports a filament of shelf water offshore. Topographic contours are overlaid in gray (50, 80, 2000, 4000 and 5000-m isobaths). The solid black contour is the 100 m isobath, generally considered the shelfbreak.

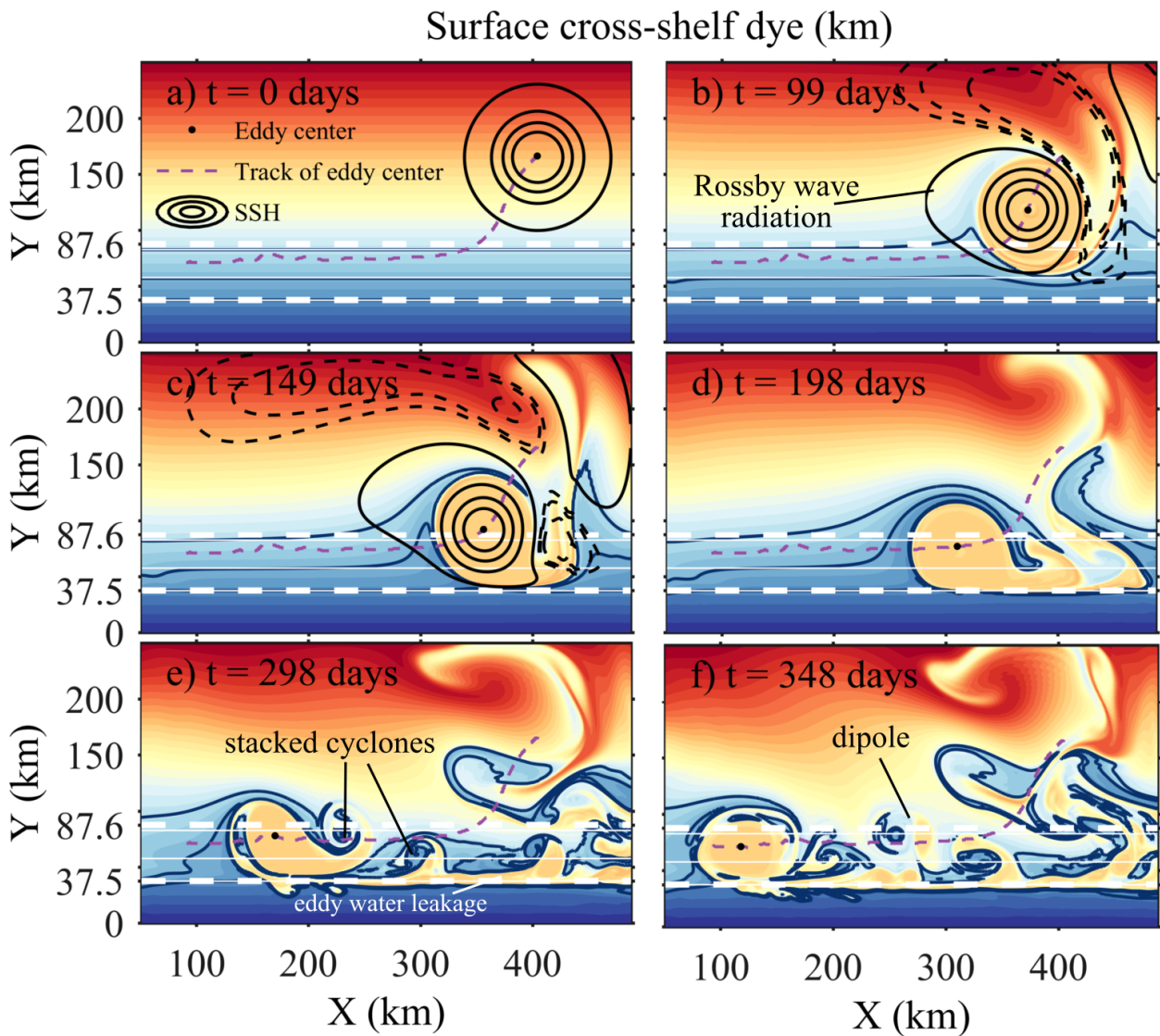


Figure 2: Snapshots of the cross-shelf dye field at the surface. Black contours are SSH, dashed contours indicate negative values. Thick white dashed lines mark the shelf- and slope-break. The evolution is just as in the flat shelf simulations of Cherian and Brink (2016).

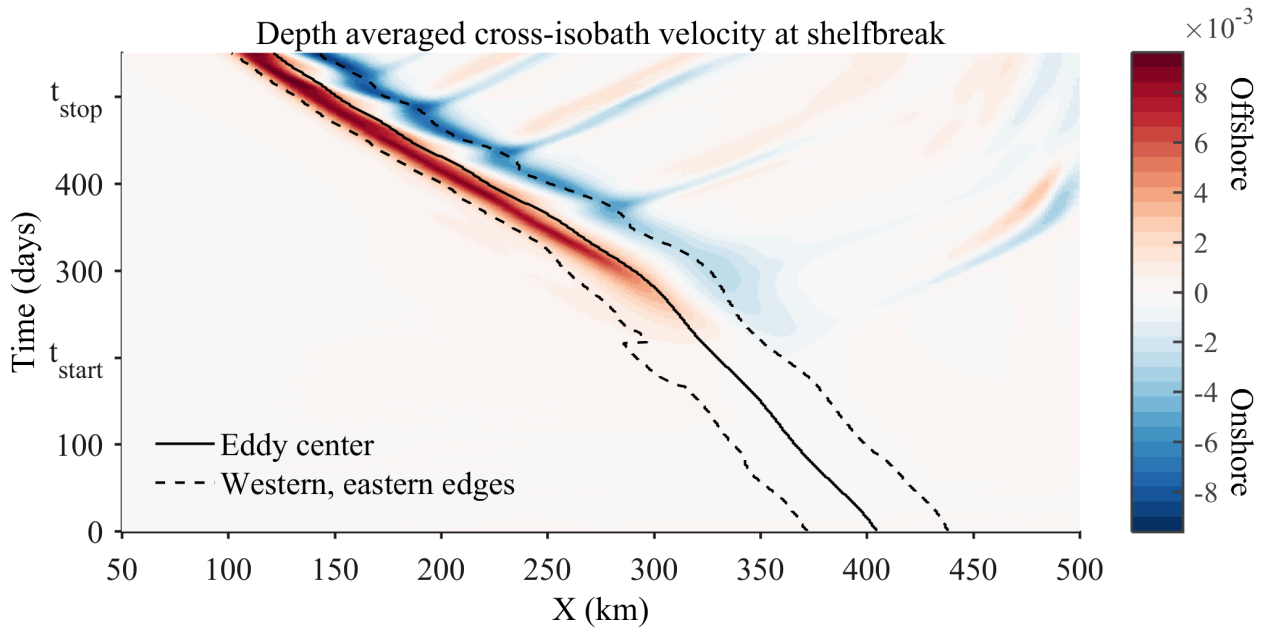


Figure 3:  $x$ - $t$  Hovmoeller diagram of depth-averaged cross-shelf velocity at the shelfbreak. Offshore flow is in red and onshore flow in blue. Solid and dashed lines respectively mark the eddy's center and its edges in the along-isobath direction. Both the offshore and onshore flow are largest near the eddy. The along-isobath scale of both the outflow and the inflow is approximately an eddy radius. Small scale anticyclones formed by the instability of the eddy water leakage propagate downstream in the coastal trapped wave direction.

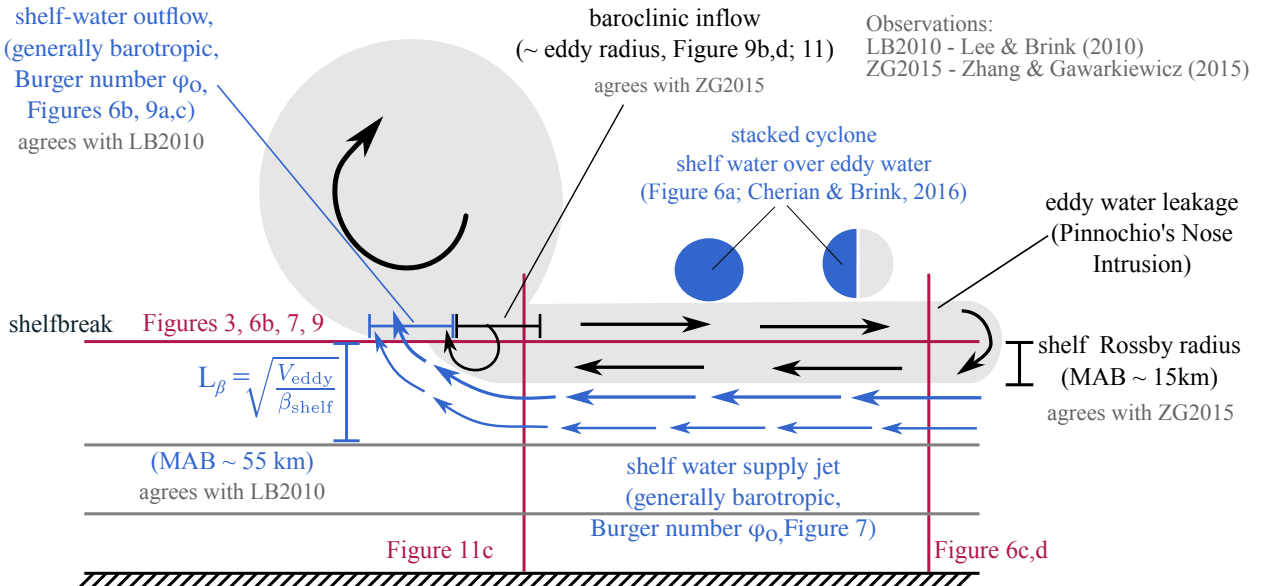


Figure 4: Schematic flowfield forced by a deep-water eddy at the shelfbreak. MAB stands for Middle-Atlantic Bight.

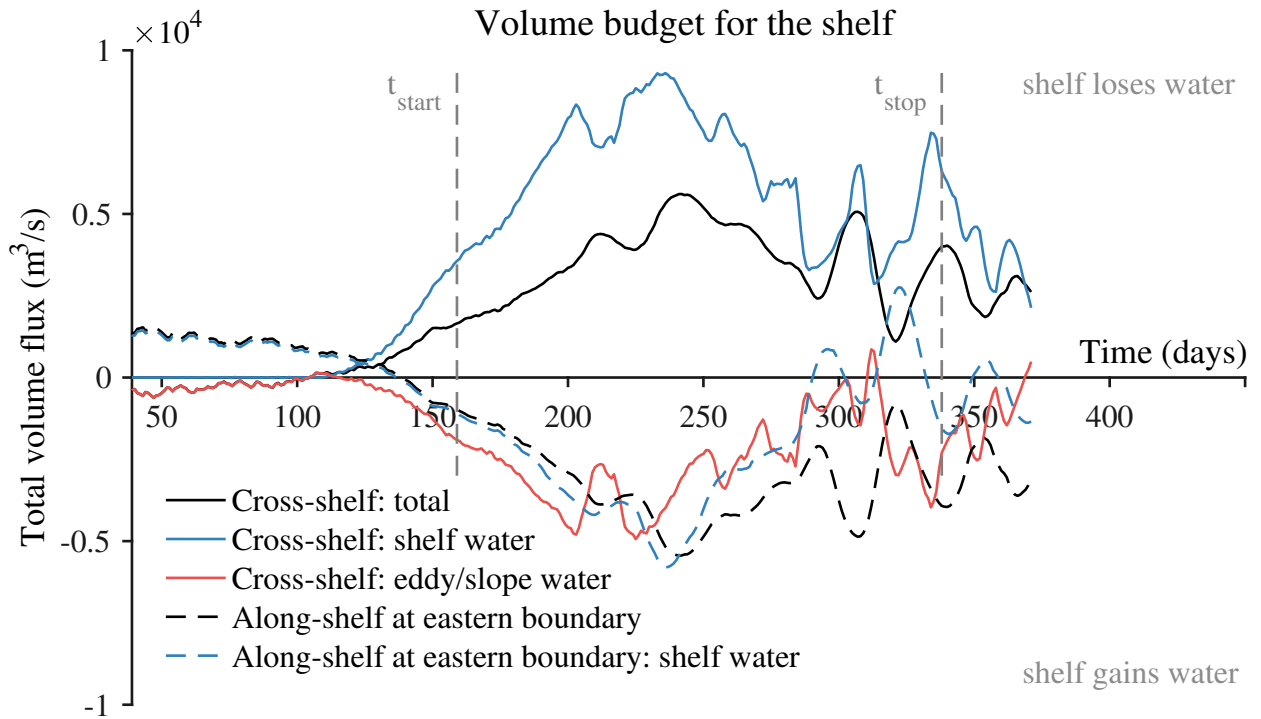


Figure 5: Volume budget for the shelf: defined as a volume bounded by the two sponges, the coastal wall and the shelfbreak. The export across the shelfbreak is compensated by an along-shelf jet moving water from the open eastern boundary into the shelf-domain, as well as the onshore flow of eddy- and slope-waters.

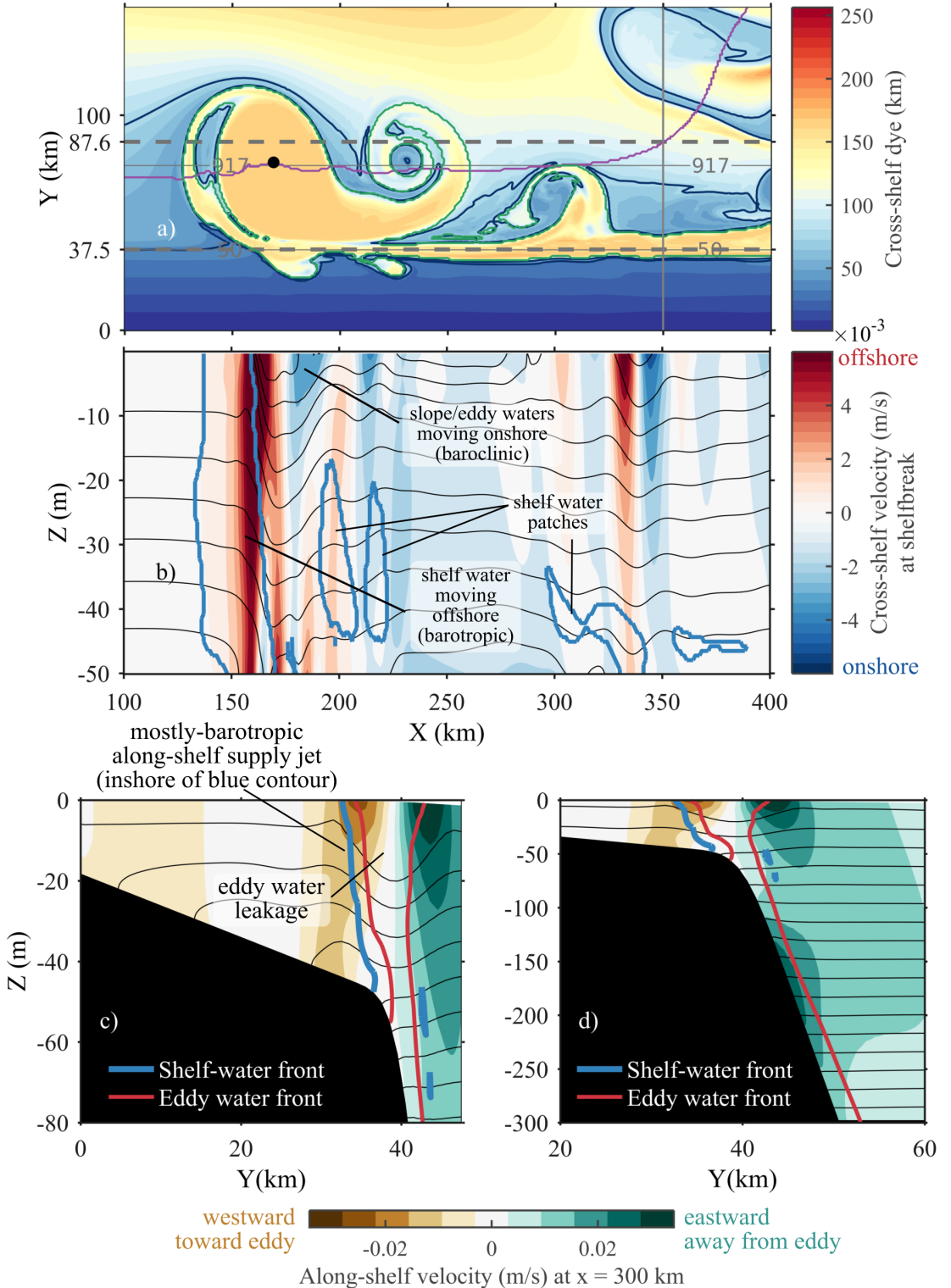


Figure 6: Instantaneous cross-sections at  $t = 300$  days from the simulation in Figure 2. (a)  $x-y$  section of cross-shelf dye at the surface. (b)  $x-z$  section of cross-shelf velocity at the shelfbreak. (c, d)  $y-z$  section of along-shore velocity at  $x = 350$  km, downstream of the eddy. Note different  $x$ -axis limits in panels (c) and (d).

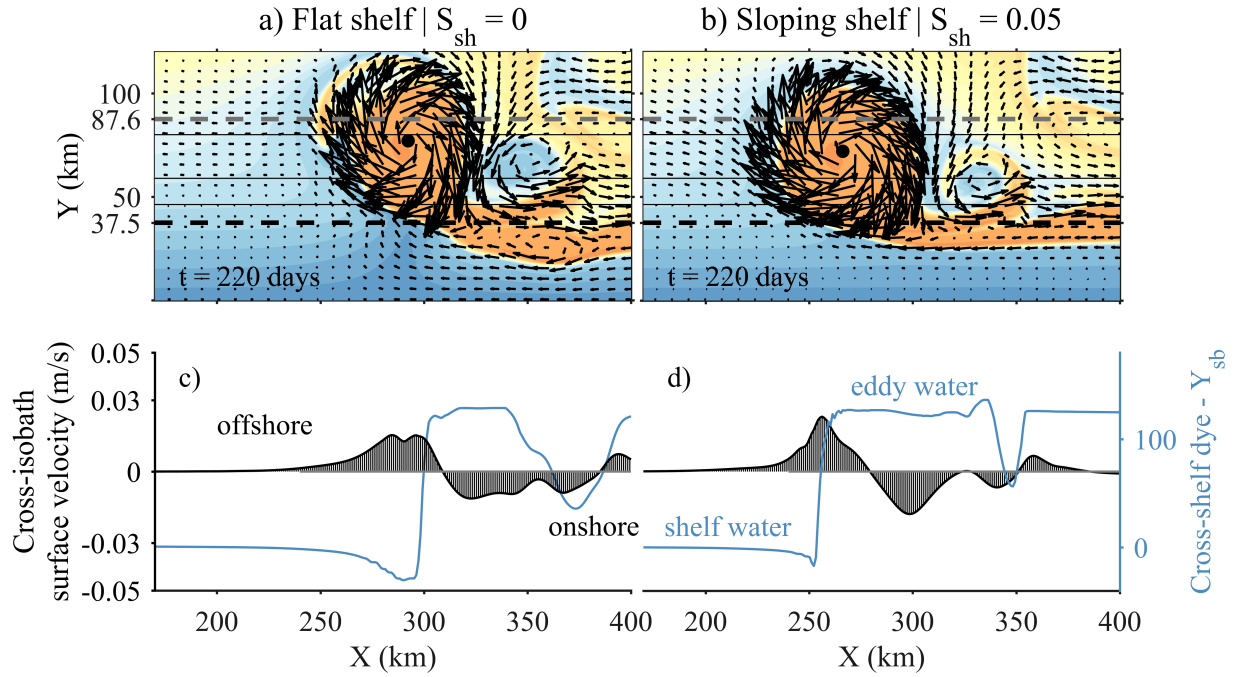


Figure 7: Horizontal velocity vectors and cross-shelf dye at the surface for a flat shelf and a sloping shelf simulation. With a flat shelf, all of the shelf is forced into motion to supply the offshore flow at the shelfbreak. With a sloping shelf, there is a limit to the extent of the eddy's influence on the shelf.

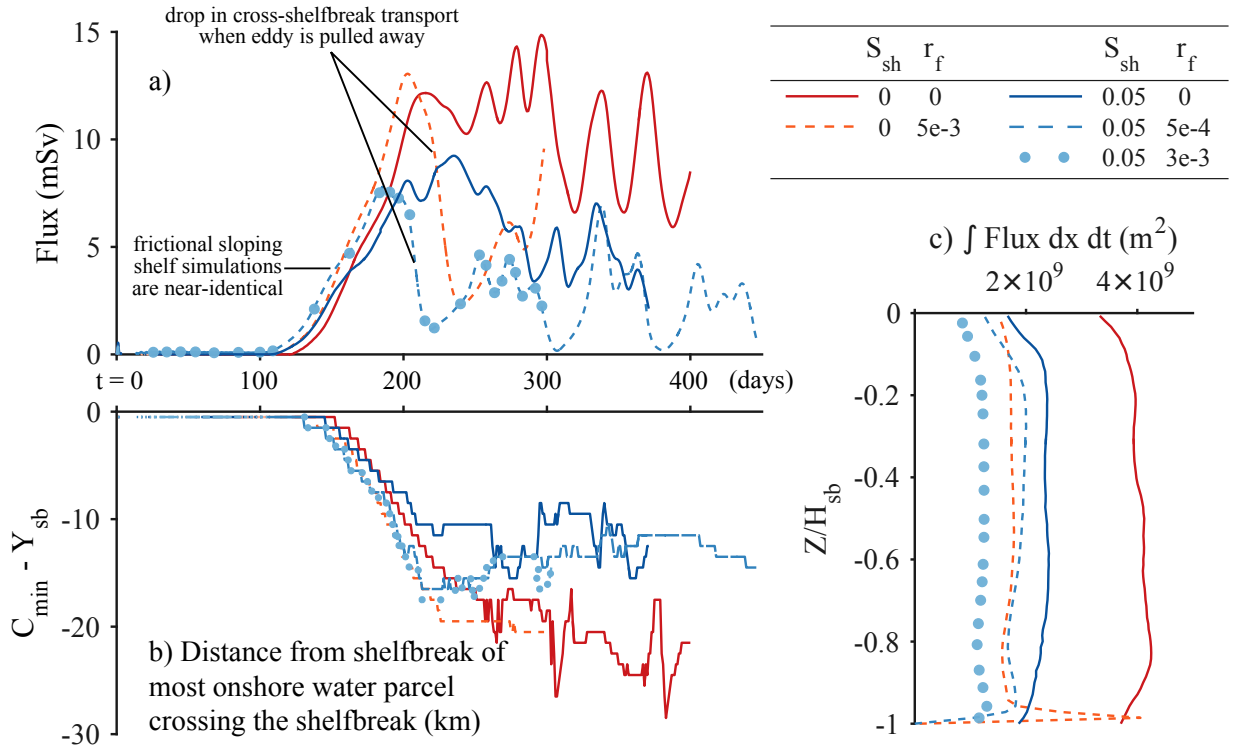


Figure 8: Offshore flow at the shelfbreak is strongly influenced by a shelf slope and not much influenced by friction. The reddish lines are for a flat shelf, and the bluish lines are for a sloping shelf. Dashes and filled circles indicate frictional simulations.  $S_{sh}$  is the slope Burger number for the shelf and  $r_f$ , the linear bottom drag coefficient in m/s. (a) Time series of offshore flux at the shelfbreak. The two frictional simulations with a sloping shelf have a nearly identical flux time series. (b) Lowest value of cross-shelf dye crossing the shelfbreak at that instant; i.e., the extent to which the eddy can extract water off the shelf. Adding a slope reduces the cross-shelf scale while increasing friction with a slope does not change much. (c) Vertical structure of the  $(x,t)$ -integrated offshore transport.

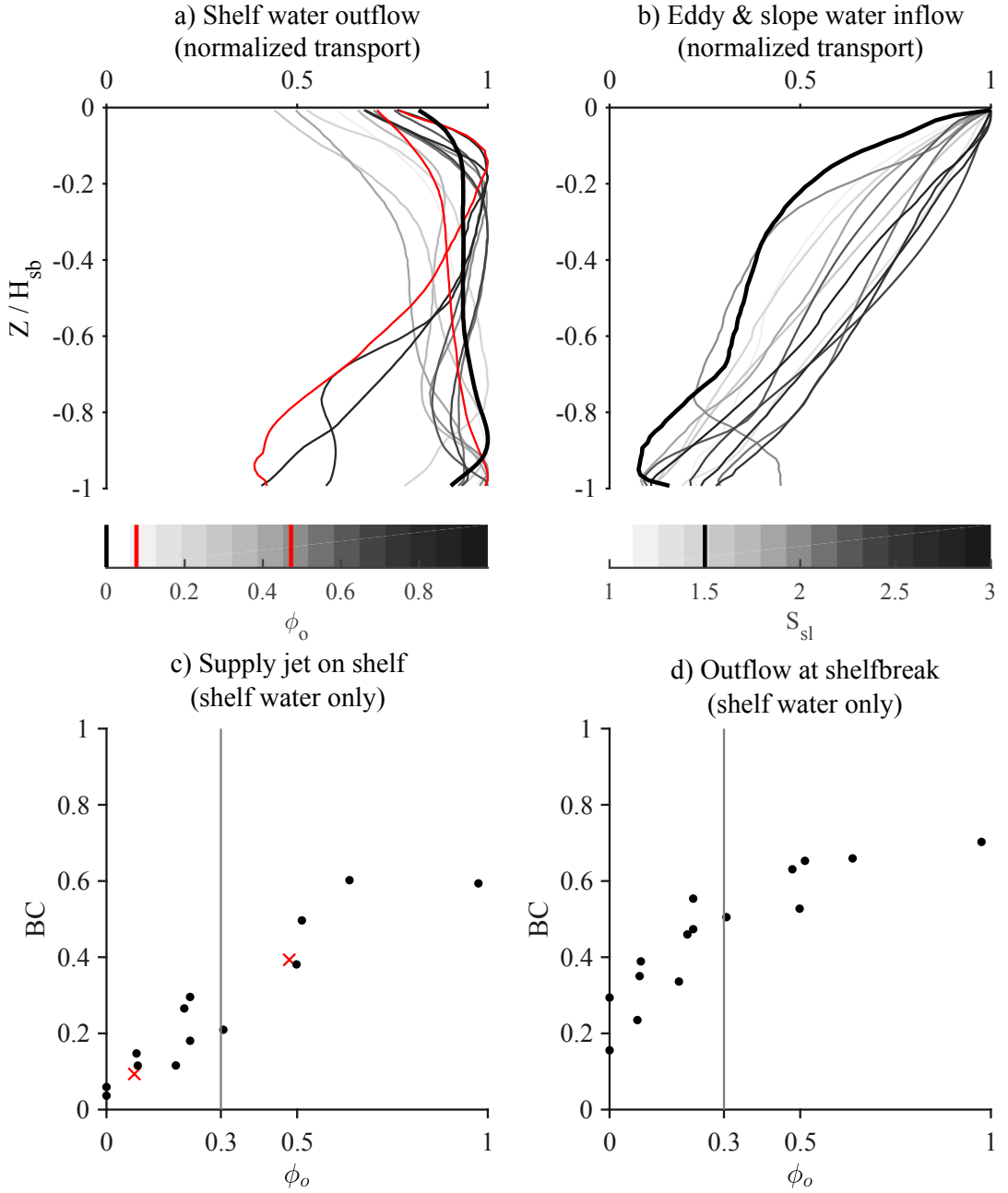


Figure 9: (a,b) Vertical profiles of the time-averaged shelf water outflow and non-shelf water inflow at the shelfbreak. The time average is over  $[t_{\text{start}}, t_{\text{stop}}]$ . The thick black lines are for a simulation with a flat shelf,  $\phi_o = 0$  and  $S_{\text{sl}} = 1.5$ . The inflow is always baroclinic while the outflow is only sometimes baroclinic (Section 5). Values are normalized such that the maximum value in each profile is 1. (c,d) The shelf water supply jet is more baroclinic, as measured by  $BC$  in equation (9), for larger values of non-dimensional parameter  $\phi_o$  (Section 5b). Two simulations with  $\lambda = 0.22$  are highlighted in red in (a) and with a red  $\times$  in (c). Despite the similarity in vertical structure of forcing, one profile is a lot more baroclinic than the other.

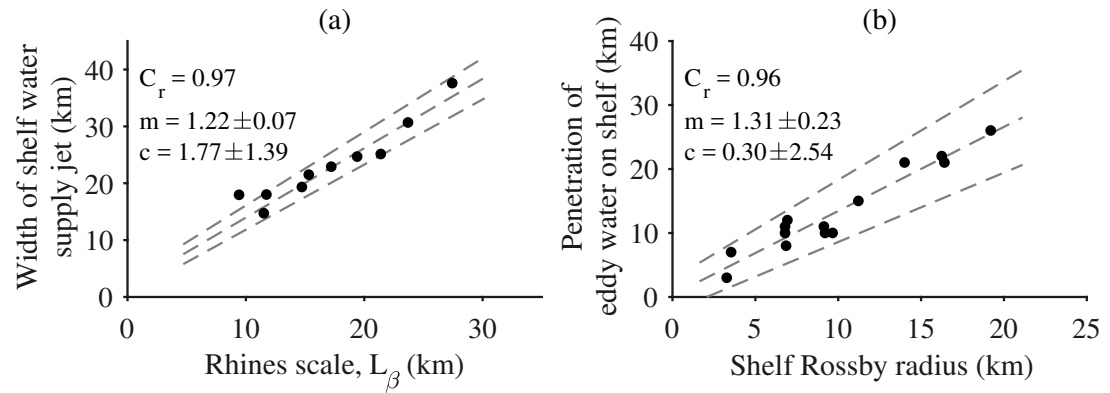


Figure 10: Parameterizations for the cross-shelf extent (a) from which the eddy can extract water from and (b) push water onto the shelf. The dashed lines are regression lines of slope  $m$  and  $y$ -intercept  $c$  and their 95% confidence bounds.  $C_r$  is the correlation coefficient.

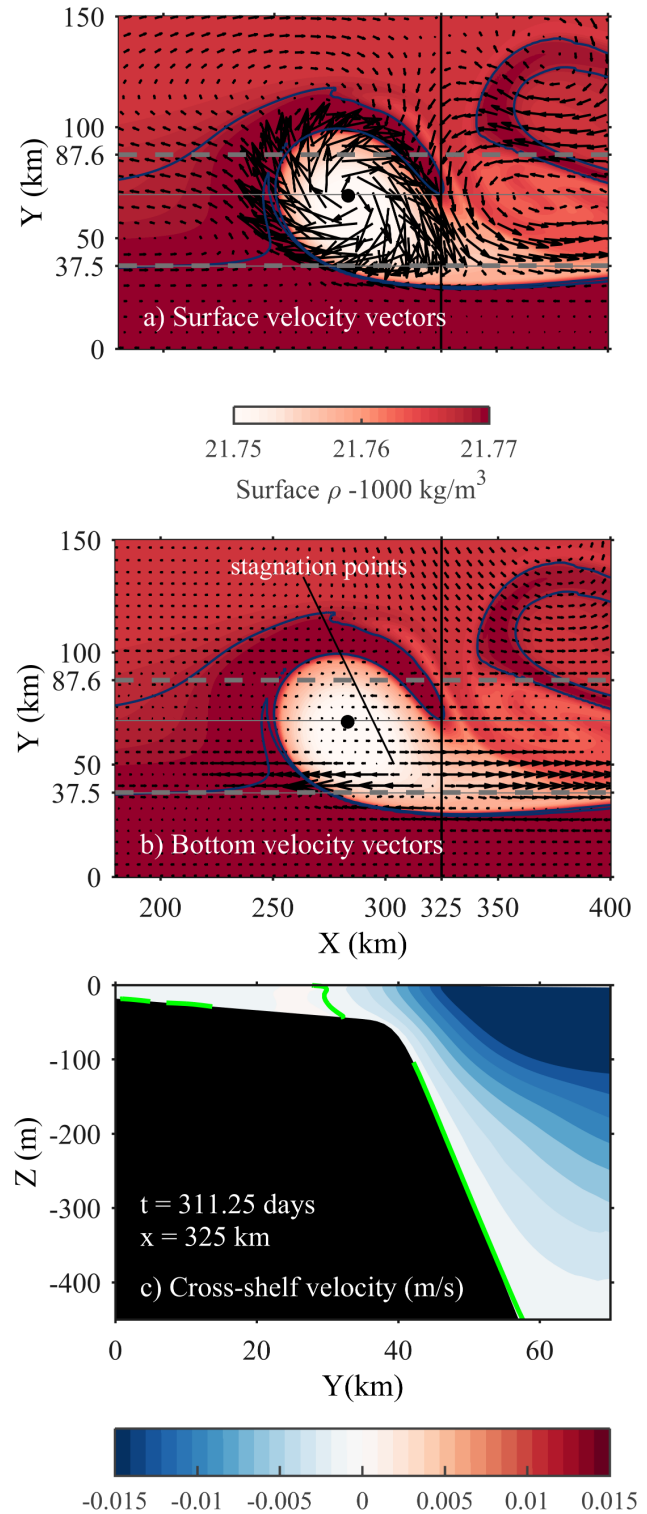


Figure 11: Snapshots for a simulation with  $\phi_o = 0.35$ . (a,b) Surface density in colour with surface and bottom velocity vectors in (a) and (b) respectively. (c) The vertical structure of cross-shelf velocity where eddy water moves onto the shelf. The thick green contour is  $v = 10^{-4} \text{ m s}^{-1}$ .

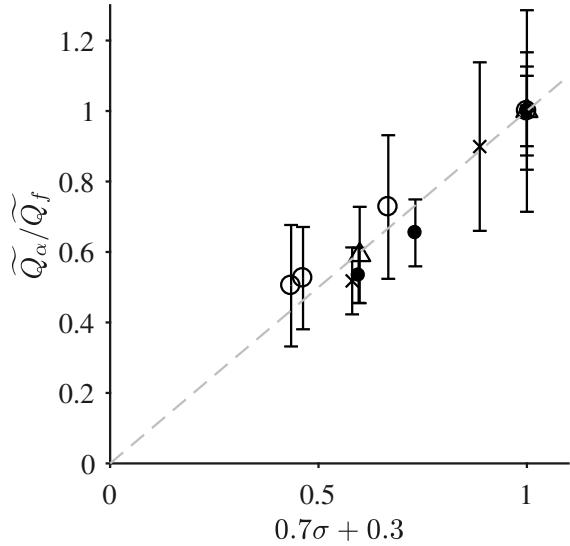


Figure 12: Increasing shelf slope reduces the cross-shelfbreak offshore flux of shelf water. The magnitude of decrease is largely explained by the change in shelf volume that the eddy can extract water from (Section 6). Markers indicate different sets of simulations. Within each set (same marker), the simulations differ only in shelf-parameters; the eddy remains the same. The different sets differ in choice of eddy parameters and  $f_0, N^2$ . The diagonal dashed line is the 45°line.

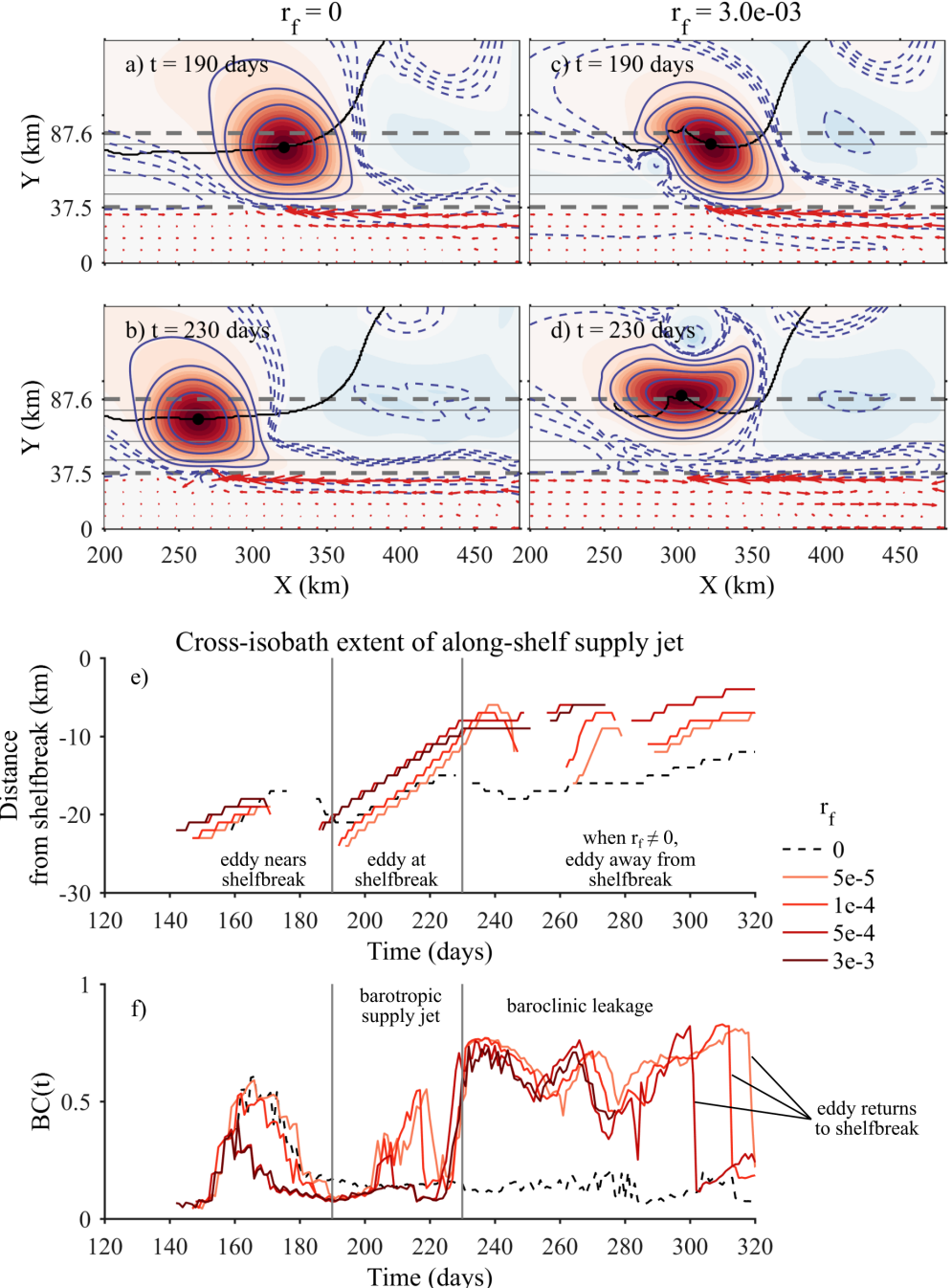


Figure 13: The influence of bottom friction. (a,b) and (c,d) are snapshots of SSH (both color and contours) and surface velocity vectors for two simulations, one with  $r_f = 0$  and the other with  $r_f = 3 \times 10^{-3}$  m s<sup>-1</sup>. Negative SSH contours are dashed. The vectors are for illustration and not comparable between panels. (e) Time series of cross-shelf scale of along-shelf flow. (f)  $BC(t)$  for the two simulations. Non-zero bottom friction coefficient spins up a strong secondary cyclone that pulls the eddy away from the shelfbreak at  $t = 230$  days, causing both a decrease in cross-shelf scale of the along-shelf flow and an increase in  $BC(t)$ .